UC San Diego
UC San Diego Previously Published Works

Title

GNSS-corrected InSAR displacement time series spanning the 2019 Ridgecrest, CA earthquakes

Permalink

https://escholarship.org/uc/item/9237s8qd

Authors

Guns, Katherine
Xu, Xiaohua
Bock, Yehuda
et al.

Publication Date

2022-03-26

DOI

10.1093/gji/ggac121

Data Availability

The data associated with this publication are available at: https://scihub.copernicus.eu/

Peer reviewed

10

11 _____

12 GNSS-corrected InSAR Displacement Time Series Spanning the 2019

13 Ridgecrest, CA Earthquakes

14

15

16

17 Katherine Guns[1†], Xiaohua Xu[2], Yehuda Bock[1], and David Sandwell[1]

18 [1]Institute of Geophysics and Planetary Physics, Scripps Institution of Oceanography, University of

19 California, San Diego, La Jolla, CA, 92093-0225

20 [2]Institute for Geophysics, University of Texas at Austin, Austin, TX, 78758

21

22 [†]Corresponding Author: Katherine Guns kguns@ucsd.edu

23

24 Date Submitted: September 21, 2021

25

26 Abbreviated Title for page heading: Ridgecrest-Spanning InSAR Time Series

27

28

29

30

31   Summary

32   InSAR displacement time series are emerging as a valuable product to study a number of earth

33   processes. One challenge to current time series processing methods, however, is that when large

34   earthquakes occur, they can leave sharp coseismic steps in the time series. These discontinuities

35   can cause current atmospheric correction and noise smoothing algorithms to break down, as

36   these algorithms commonly assume that deformation is steady through time. Here, we aim to

37   remedy this by exploring two methods for correcting earthquake offsets in InSAR time series: a

38   Simple Difference Offset Estimate (SDOE) process and a Multiparameter Offset Estimate

39   (MPOE) parametric time series inversion technique. We apply these methods to a two-year time

40   series of Sentinel-1 interferograms spanning the 2019 Ridgecrest, CA earthquake sequence.

41   Descending track results indicate that the SDOE method precisely corrects for only 20% of the

42   coseismic offsets at 62 study locations included in our scene and only partially corrects or

43   sometimes overcorrects for the rest of our study sites. On the other hand, the MPOE estimate

44   method successfully corrects the coseismic offset for the majority of sites in our analysis. This

45   MPOE method allows us to produce InSAR time series and data-derived estimates of

46   deformation during each phase of the earthquake cycle. In order to better isolate and estimate the

47   signal of postseismic lithospheric deformation in the InSAR time series, we apply a GNSS-based

48   correction to our interferograms. This correction ties the interferograms to median-filtered

49   weekly GNSS displacements and removes additional atmospheric artifacts. We present InSAR-

50   based estimates of postseismic deformation for the area around the Ridgecrest rupture, as well as

51   a two-year coseismic-corrected, GNSS-corrected InSAR time series dataset. This GNSS-

52   corrected InSAR time series will enable future modeling of postseismic processes such as

53   afterslip in the near field of the rupture, poroelastic deformation at intermediate distances, and

54   viscoelastic deformation at longer time scales in the far field.

55

56   Keywords: Satellite geodesy, Seismic cycle, Transient deformation, Time-series analysis, North

57   America

58

59

60

61

62   1. Introduction

63   The rise of high precision, satellite-based geodetic measurements over the last three decades has

64   allowed us to better understand the Earth system in a variety of ways (Burgmann & Thatcher,

65   2013; Bock & Melgar, 2016; Biggs & Wright, 2020). Using both Global Navigation Satellite

66   System (GNSS) and Synthetic Aperture Radar (SAR) observations of the surface, we can

67   quantify hydrologic loading processes in the hydrosphere and cryosphere (e.g., Argus *et al.*

68   2005*; Chaussard et al.* 2014*; Neely et al.* 2021; Bock & Wdowinski, 2021), magmatic processes

69   at active volcanic centers (e.g., Berardino *et al.* 2002; Poland *et al.* 2006), landslide processes

70   (e.g., Hilley *et al.* 2004; Tong & Schmidt, 2016; Handwerger *et al.* 2019; Bekaert *et al.* 2020; Hu

71   *et al.*, 2020), and earthquake cycle processes (e.g., Bürgmann *et al.* 2000; Wei *et al.* 2011; Weiss

72   *et al.* 2020; Xu *et al.* 2021) with continually improving temporal and spatial resolution. For SAR

73   methods in particular, the ongoing European Space Agency Copernicus Sentinel-1 mission

74   provides open-access data with excellent coverage around the globe at increased temporal

75   resolution compared to previous missions. This reliable dataset of SAR images, in combination

76   with improved processing strategies for Interferometric SAR (InSAR), has enabled the

77   production of precise displacement time series, which are proving to be an invaluable tool for

78   assessing deformation over time (Hooper *et al.* 2012). Some researchers calculate long-term

79   average velocities from InSAR time series in order to analyze different deformation signals (e.g.,

80   Bürgmann *et al.* 2005; Dixon *et al.* 2006; Weiss *et al.* 2020), while others rely on the

81   displacement over time to illuminate the temporal evolution of a particular process (Hetland *et*

82   *al.* 2012; Chaussard *et al.* 2014; Xu *et al.* 2018; Tymofyeyeva *et al.* 2019; Klein *et al.* 2019).

83   Due to high spatial resolution, InSAR time series can sharpen the picture of interseismic

84   deformation and fault creep, as GNSS motions, even in areas of close station spacing, are not as

85   effective at illuminating discontinuities in surface displacements across faults (Tong *et al.* 2013;

86   Shirzaei & Bürgmann, 2013; Fattahi & Amelung, 2016).

87

88   Processing InSAR time series often relies on a fundamental assumption that all deformation

89   present in the time series is relatively steady over time. This assumption enables the effective

90   correction of atmospheric errors and other noise sources (Tymofyeyeva & Fialko, 2015; Xu *et al.*

91   2017). A seismic event that is large enough to register displacement at the surface however,

92   introduces an abrupt step into the time series, which then causes time series processing and

93   smoothing algorithms to break down. Some researchers even use these abrupt steps in pixel time

94   series to search for smaller and less conspicuous earthquakes in interferograms (e.g., Grandin *et*

95   *al.* 2017; Liu *et al.* 2021). Hetland et al. (2012) have developed a computer code to explicitly

96   deal with earthquake offsets and other time-dependent processes (known as MInTS). Here we

97   refine their approach with application to the July 2019 Ridgecrest earthquakes.

98

99   The July 4th, 2019 M_W 6.4 and July 5th, 2019 M_W 7.1 Ridgecrest earthquakes ruptured a

100   previously unmapped series of faults (e.g., Ponti *et al.* 2020) in the eastern California Mojave

101   desert (Fig. 1), and was one of the most well-observed earthquake sequences in recent history.

102   These events allowed the active tectonics community a detailed firsthand look at a number of

103   earthquake processes, including postseismic deformation (viscoelastic relaxation, afterslip, and

104   poroelastic effects; e.g., Wang & Bürgmann, 2020), aftershock patterns (e.g., Hardebeck, 2020),

105   mechanical fault structure and behavior in the rupture zone (e.g., Plesch *et al.* 2020; Xu *et al.*

106   2020a,b; Milliner *et al.* 2021), and possible impact on nearby fault zones (e.g., Ross *et al.* 2019).

107   In addition, the location of these earthquakes has favorable conditions for InSAR analysis,

108   including an arid climate and a high coherence desert landscape lacking in vegetation.

109

110   To best estimate the coseismic offset introduced by the Ridgecrest earthquake sequence, we

111   explore two methods to estimate coseismic displacements within InSAR time series: (1) a

112   straightforward Simple Difference Offset Estimate (SDOE) approach and (2) a Multiparameter

113   Offset Estimate (MPOE) time series estimate approach. We additionally use our coseismic-

114   corrected time series to calculate an estimate of the cumulative postseismic deformation

115   following the two mainshock events. To further improve our estimates of postseismic

116   deformation, we use the dense network of GNSS stations in the area to incorporate a GNSS-

117   based correction to our InSAR time series. This correction mainly helps mitigate large spatial-

118   scale (long wavelength) atmospheric errors, but also helps provide an underlying spatial

119   reference for the InSAR deformation. When used together, InSAR and GNSS displacement time

120   series can better illuminate ongoing processes than either dataset alone, and we create a final

121   product of GNSS-corrected, coseismic-corrected InSAR time series. In addition, by utilizing our

122   MPOE time series estimate method, we produce a series of map-view earthquake cycle products

123 that delineate the interseismic, coseismic, and postseismic periods of the earthquake cycle from

124 InSAR time series.

125
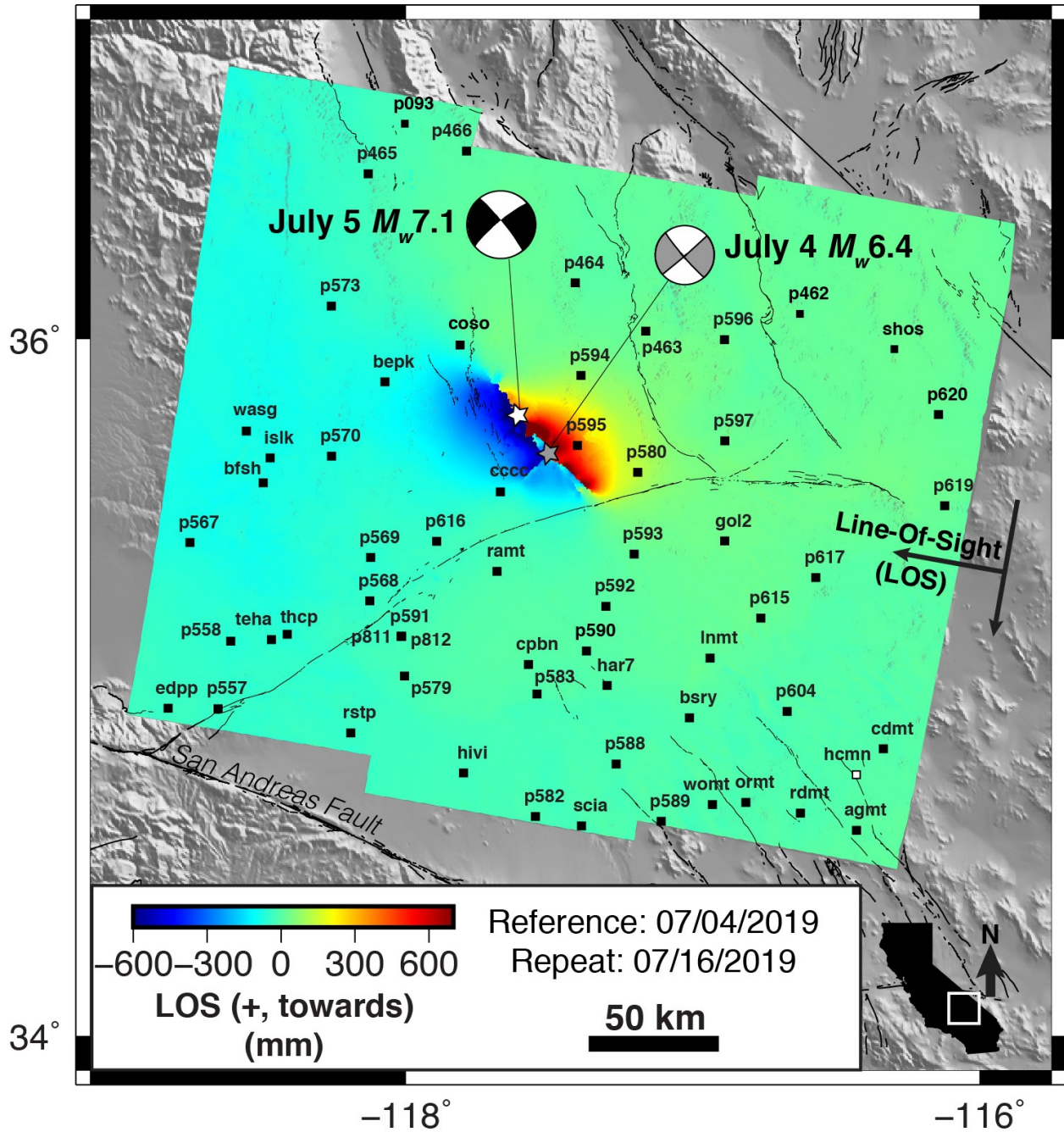
Figure 1. Unwrapped descending track 071 Sentinel-1 interferogram illustrating the coseismic and early

postseismic displacements of the July 2019 Ridgecrest earthquake sequence in satellite Line-Of-Sight

(LOS), where red (positive) means motion towards the satellite. Locations of GNSS stations labeled by

130   their 4-character station codes. In future plots we reference interferograms to the location of station

131   HCMN (white square, lower right). Focal mechanism nodal planes from USGS Earthquake catalog.

132   2. Methods

133

134   2.1 InSAR Processing

135   To incorporate the displacements introduced by the Ridgecrest sequence into InSAR time series

136   analyses, we start by processing 90 descending track images through the time period of July

137   2018 to July 2020, and 79 ascending track images through the time period of November 2018 to

138   July 2020, all with repeat times between 6 and 12 days. We center our analysis on scenes that

139   cover the area around the Ridgecrest rupture, which were collected by the C-Band Sentinel-1

140   satellites operating in Terrain Observation by Progressive Scan (TOPS) mode across descending

141   track 71 and ascending track 64. We download Single Look Complex (SLC) data files from the

142   Alaska Satellite Facility and process them using GMTSAR version 6.1 (Sandwell *et al.* 2016)

143   and begin by aligning all secondary scenes to a single reference image chosen through visual

144   inspection of a perpendicular baseline-versus-time plot (Fig. S1). This coregistration process is

145   described in detail by Xu et al. (2017) and takes a geometric approach that increases the accuracy

146   of pixel alignment and improves phase recovery.

147

148   We calculate interferograms for each of the three TOPS subswaths of the aligned set of images,

149   and then merge the products in radar coordinates to create a full scene interferogram for each day

150   pair that falls within a $\leq$ 50-day temporal baseline and a $\leq$ 100-m spatial perpendicular baseline

151   and low-pass filter them at 200 m wavelength. Once we have our merged interferograms, we

152   unwrap the phase of each pair using the Statistical-Cost, Network-Flow Algorithm for PHase

153   Unwrapping (SNAPHU) program (Chen & Zebker, 2002; Agram & Zebker, 2009) implemented

154   within the GMTSAR package. We apply a large phase discontinuity threshold to allow for the

155   displacements observed during the Ridgecrest sequence. To remove areas of poor coherence

156   from the unwrapping process, we create a mask of common points of poor coherence throughout

157   our stack of interferograms that excludes small areas in the neighboring Sierra Nevada and

158   Central Valley (mainly bodies of water and areas of snow cover and agriculture). This process

159   produces a set of 415 descending track unwrapped interferograms and 389 ascending track

160   unwrapped interferograms. One of our descending track unwrapped interferograms showing

161   coseismic motion is presented in Fig. 1, and is formed from the closest pair of images to

162   encompass the Ridgecrest earthquake sequence, July 4th, 2019 and July 16th, 2019. In this study,

163   we primarily focus our analysis on the descending track interferograms due to the lower levels of

164   noise present in the data collected in the morning (versus the ascending track which is collected

165   in the late afternoon).

166

167   2.2 Time Series Processing

168   For calculating a time series from our unwrapped interferograms, we use the coherence-based

169   Small Baseline Subset (SBAS) approach (Berardino *et al.* 2002; Schmidt & Bürgmann, 2003;

170   Tymofyeyeva & Fialko, 2015; Tong & Schmidt, 2016; Xu *et al.* 2017; Xu *et al.* 2021)

171   implemented within GMTSAR. This SBAS approach takes in coherence values of the

172   interferograms as weights in a least-squares inversion for time series at every pixel, instead of

173   removing low-coherence pixels altogether (Xu *et al.* 2017). To prepare for SBAS processing we

174   further downsample unwrapped interferograms to 32 pixels in range (32 pixel spacing using a

175   bicubic interpolation in GMT) and 8 pixels in azimuth (8 pixel spacing using a bicubic

176   interpolation in GMT) to save storage space and computation time, and reference our descending

177   track interferograms to a stable reference point located >120 km southeast of the Ridgecrest

178   rupture zone at the location of continuous GNSS station HCMN (see white square in Fig. 1).

179

180   The first step we take is to run SBAS for our interferograms with no temporal smoothing or

181   correction parameters. This produces a displacement time series in Line of Sight (LOS) that

182   includes both the discontinuous coseismic offset from the Ridgecrest earthquake sequence, as

183   well as the postseismic deformation that followed the main event (Fig. 2). A common next step

184   in calculating InSAR time series with SBAS is to apply a temporal smoothing constraint (e.g.,

185   Schmidt & Bürgmann, 2003), which has been shown to successfully reduce noise and correct for

186   propagation delays through the troposphere and the ionosphere using a Common-scene Stacking

187   (CSS) approach (Tymofyeyeva & Fialko, 2015; Xu *et al.* 2017). Both the CSS correction and

188   any chosen smoothing constraint however, include a primary assumption that all displacements

189   in the time series are steady over the time span of observation of the series. To illustrate the

190   adverse effects of applying this correction we apply it to our set of interferograms. The effect of

191   temporal smoothing and the CSS correction across the sharp coseismic step is immediately

apparent (Fig. 2B). The correction spreads the sharp displacement jump across more than fifteen

displacement time steps, which does not accurately capture the deformation caused by the

earthquake rupture. Thus, to properly apply any smoothing constraints, we will first need to

remove the coseismic displacement.
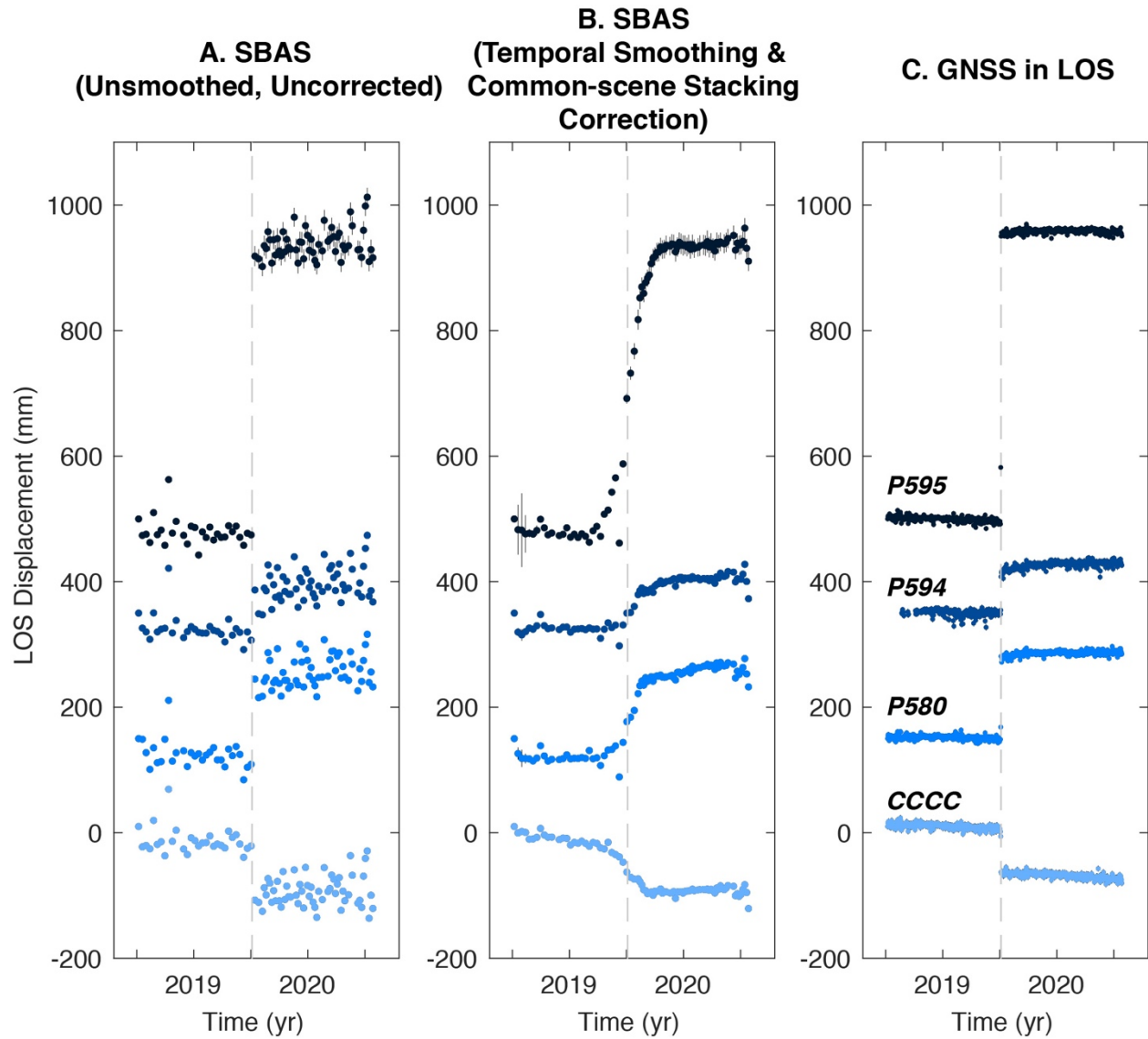
Figure 2. InSAR time series at the locations of four GNSS stations near the Ridgecrest rupture produced

through the Small Baseline Subset (SBAS) method with (A) no temporal smoothing or correction, (B)

temporal smoothing and the CSS correction applied; (C) GNSS time series in Line-of-Sight (LOS) for

comparison. Uncertainties for InSAR time series calculated as a standard deviation of a 10x10 pixel area

around the station location point. Grey dashed lines represent the occurrence of the Ridgecrest earthquake

sequence.

204

205   2.3 Estimating Time Series Motions

206

207   2.3.1 GNSS Time Series

208   To quantify long term velocities and postseismic displacements for specific locations across our

209   InSAR scenes for comparison between InSAR and GNSS displacement time series, we apply a

210   parametric time series model commonly used in GNSS time series processing (Nikolaidis, 2002;

211   Bevis & Brown, 2014; Bock & Melgar, 2016). We start by using the Extended Solid Earth

212   Science ESDR System (ESESES) daily Combination time series (Clean Weighted Mean

213   Combination, removed of non-tectonic offsets, 08/10/2021 Solution) (http://sopac-

214   csrc.ucsd.edu/index.php/displacements/) produced as part of NASA's Making Earth System Data

215   Records for Use in Research Environments (MEaSUREs) program (Bock *et al.* 2021). The

216   combination time series are estimated from independent analyses of the GNSS data by Scripps

217   Institution of Oceanography and Jet Propulsion Laboratory using a common source of metadata.

218   We crop the GNSS time series to the time period of our InSAR time series (2018.5000 to

219   2020.5000) and project the time series observations for each station into LOS. We then use a

220   least squares inversion, weighted by the LOS-projected GNSS uncertainties, to estimate our

221   parametric terms as follows:

222

223     $$D(t) = A_1 + A_2 * t + A_3 \sin(2T_1 t) + A_4 \cos(2T_1 t) + A_5 \sin(2T_{0.5} t) + A_6 \cos(2T_{0.5} t)$$

224     $$+ \left[A_7 * H\left(t - t_{M6.4eq}\right) \right] + \left[A_8 * H\left(t - t_{M7.1eq}\right) \right] + \left[A_9 \left(1 - e^{-\frac{\Delta t}{\tau}}\right) * H\left(t - t_{eq}\right) \right] \quad [1]$$

225

226   where $D(t)$ represents total displacements present at a given time t, and $H\left(t - t_{eq}\right)$ is the

227   Heaviside function, where t_{eq} is equal to the respective time (in decimal year) of the $M_W 6.4$ or

228     $M_W 7.1$ event. Numbered parameters correspond to initial position (A_1), velocity (A_2), seasonal

229   terms for annual (T_1 = 1 year) and semiannual ($T_{0.5}$= ½ year) periods (A_3 - A_6), the Ridgecrest

230   coseismic offsets (A_7 - A_8), and an exponential postseismic term for the Ridgecrest earthquake

231   sequence (A_9) using a characteristic relaxation time (τ) of 182.5 days (half year). These terms are

232   the same terms solved for in the MEaSUREs time series analysis of daily displacement. LOS-

233   projected GNSS station displacements and their final models are presented in Fig. S2 for ten

234   representative stations. We use the estimated exponential term amplitude from the model to

235   calculate a cumulative postseismic displacement over the two months directly following the

236   earthquake sequence (see Table 1).

237

238   2.3.2 InSAR Time Series for Individual Pixels

239   When we estimate a time series model from the SBAS-produced InSAR time series for any

240   given pixel, we apply an approach similar to that of Hetland et al. (2012) and Neely et al. (2021)

241   that estimates similar model terms to the GNSS time series parametric model in [1]:

242

243 $$D(t) = A_1 + A_2 * t + \left[A_3 * H\left(t - t_{eq}\right)\right] + \left[A_4\left(1 - e^{-\frac{\Delta t}{\tau}}\right) * H\left(t - t_{eq}\right)\right] \quad [2]$$

244

245   For the InSAR time series however, we make three adjustments to equation [1] to produce

246   equation [2]: (1) estimate only a single combined coseismic offset for both main Ridgecrest

247   events instead of two (given the lack of temporal resolution for InSAR scenes compared to daily

248   GNSS solutions); (2) we do not estimate seasonal terms on InSAR time series due to both the

249   short 2-year time span of our time series and the high levels of noise, as the seasonal term can

250   then further bias the coseismic offset estimate; and (3) we use a non-weighted least squares

251   solution to estimate the final model terms. The non-weighted framework here is due to the lack

252   of accurate estimated uncertainties for each pixel, a challenge that is an active area of research

253   (e.g., Tong *et al.* 2013; Agram & Simons, 2015). Estimating a time series model is our primary

254   means of constraining each deformation phase in the earthquake cycle directly from the InSAR

255   time series, which we compare with estimates from the GNSS time series.

256

257   2.4 Incorporating Coseismic Displacement

258

259   2.4.1 Simple Difference Offset Estimate (SDOE) Correction

260   In order to account for the coseismic offset caused by the earthquake events, we first calculate an

261   unsmoothed SBAS time series for the set of interferograms, resulting in a sharp step in

262   interferograms spanning the earthquakes as shown in Fig. 2A. We isolate the deformation

263   primarily caused by the coseismic rupture by subtracting the first SBAS-produced displacement

264   grid after the earthquake from the displacement grid just before the earthquakes to create a

265   gridded coseismic estimate, or our SDOE grid (Fig. 3A). This is the simplest way to estimate the

266   coseismic offset, and is computationally quick and efficient. This resulting grid is then subtracted

267   from all interferograms pairs that span the earthquakes (Fig. 3A). We then run SBAS using all

268   the original downsampled interferograms, but with the replacement of the ten earthquake-

269   spanning interferograms that have the SDOE estimate grids removed. Since postseismic

270   displacements, which gradually decay with time, are small compared to the coseismic

271   displacements for the Ridgecrest earthquake sequence (Jin & Fialko, 2020), we can then apply

272   the CSS correction to this time series dataset in order to reduce the levels of noise from

273   atmospheric propagation delay (Tymofyeyeva & Fialko, 2015). Applying the CSS correction has

274   been successful for seasonal signals (Tymofyeyeva & Fialko, 2015), which vary over time scales

275   that are smaller than the decaying exponential signal of a postseismic signal. The results of this

276   approach are illustrated in Fig. 4A for four different stations near the Ridgecrest rupture.

277

278
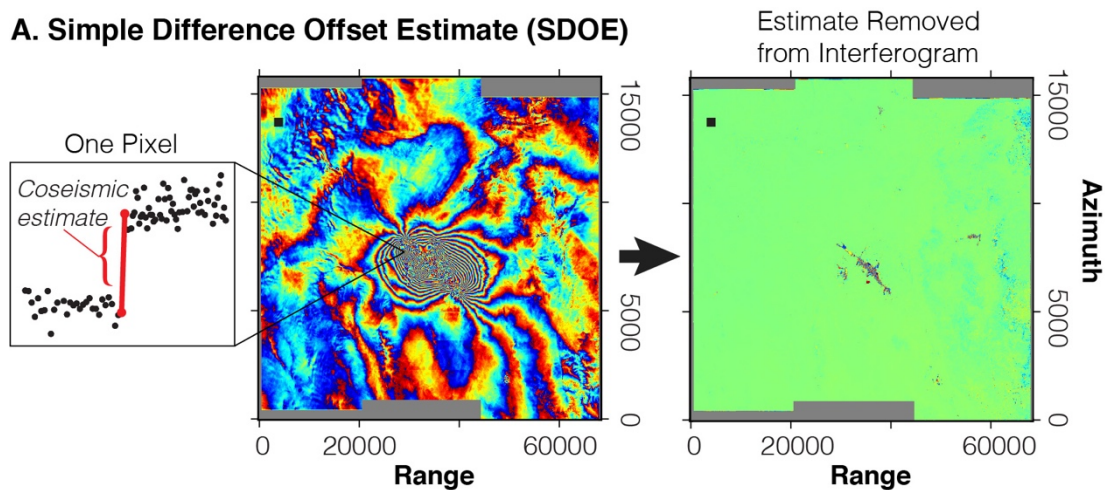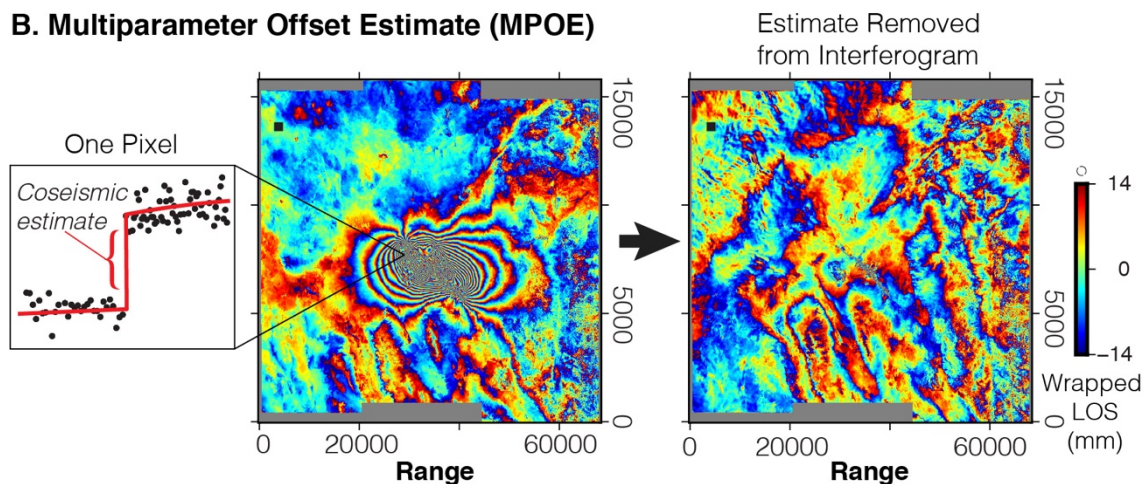
Figure 3. Two trial methods of correcting the coseismic displacement from the Ridgecrest earthquake sequence, presented in radar coordinates, which appear as though 180º flipped from geocoordinates; (A) shows our Simple Difference Offset Estimate (SDOE) calculated by differencing the SBAS-produced displacement grids bracketing the earthquake, and the result of subtracting that estimate grid from the descending 07/04/2019—07/16/2019 coseismic interferogram while (B) shows our Multiparameter Offset Estimate (MPOE) grid calculated through a pixel-by-pixel time series estimation process, as well as the result of subtracting this MPOE estimate from the interferogram. The MPOE correction removes the coseismic signal and leaves behind the noise, while the SDOE correction removes both coseismic signal and noise, which can then lead to artificial over-corrections of the coseismic offset. Black square is the reference point in the eastern Mojave Desert.

2.4.2 Multiparameter Offset Estimate (MPOE) Correction

Our second coseismic correction test case implements a Multiparameter Offset Estimate (MPOE) correction. We calculate this correction grid by estimating a parametric time series model (using equation [2] of Section 2.3.2) for each pixel's time series from an SBAS-produced InSAR displacement grid set using an approach similar to Hetland et al. (2012), but using only a least-squares inversion instead of wavelet decomposition analysis. This parametric model estimates an initial position, a velocity, an exponential postseismic term with a relaxation time (τ) value of a half year, and, most importantly, a coseismic offset. This approach allows us to estimate the coseismic offset using the entire InSAR time series (N = 71 epochs) rather than just the single time epoch before and single time epoch after the events, and thus is able to suppress noise more effectively; however, it requires a more complex coding approach and takes more time to compute. Similar methods, including fitting a line to a groups of displacement epochs just before and just after the event, could also improve the resolvability for smaller events (e.g., Liu *et al.* 2021). Once we have a coseismic estimate for every grid pixel, we remove that MPOE grid from each of our ten earthquake-spanning interferograms (Fig. 3B). We then run another SBAS to calculate MPOE coseismic-corrected time series displacement grids. The results of this approach are illustrated in Fig. 4B.

3. Results

To determine which of our two coseismic correction methods produces the best result using the descending track time series dataset, we compare the coseismic offsets estimated using our time

310   series analysis (section 2.3.2) before the correction and after the correction, for the 62 specific

311   pixels that correspond to the locations of GNSS stations. We find that while the SDOE correction

312   works fairly well for some pixels, the MPOE correction grid produces better results overall (Fig.

313   4). When we apply the SDOE correction to our InSAR time series, we find that 80% of our 62

314   comparison pixels' time series still have some residual visible estimated coseismic offset,

315   varying in magnitude from 5 - 36 mm. In addition, at certain station locations, the SDOE

316   correction produces an anomalous coseismic offset. This offset is introduced as an effect of both

317   the noise present in the InSAR data and the fact the SDOE coseismic correction is an exact

318   difference between two time series data points, rather than a difference between model-derived

319   displacements that are estimated from all data points. The pixel at the location of GNSS station

320   P594 illustrates this effect in Fig. 4. Within Fig. 2, we see that, in LOS displacement, the

321   Ridgecrest earthquake caused the location of station P594 to move towards the satellite (a

322   positive offset); yet when we apply the SDOE coseismic correction, the pixel at station P594

323   shows a residual, negative coseismic offset in the estimated time series (Fig. 4A). This is a

324   consequence of differencing a time series displacement point at the bottom of the pre-earthquake

325   spread of data with a displacement point at the top of the post-earthquake spread, effectively

326   introducing an artificial offset of the approximate size of the spread or noise of the data. The fact

327   that this epoch-to-epoch SDOE approach is so affected by noise indicates that, while it is simple

328   and fast to compute, it is not a feasible method for accomplishing an accurate coseismic

329   displacement estimate in our InSAR time series.

330

331   By taking the spread of noise into account in our coseismic estimates with the MPOE method

332   however, we are able to more accurately correct the InSAR time series for the Ridgecrest

333   earthquakes offset. This is most visible by directly comparing the InSAR time series for stations

334   P580 and P594 in Figs 4A and 4B (black circles). By applying a more accurate correction, this

335   approach allows us to apply temporal smoothing and the CSS correction with more confidence,

336   now that the sharp, large-magnitude displacements have been removed. We choose to apply this

337   coseismic correction going forward and we refer to this MPOE-corrected data as our "coseismic-

338   corrected" time series.

339

340   In our coseismic corrected time series set, 24 pixels at GNSS station locations exhibit the

341   behavior similar to that shown by station P580's time series in Fig. 4B, wherein there is a small

342   amount of apparent coseismic offset still fit by the time series model after the coseismic

343   correction is applied. Fifteen (24%) of these 62 pixels show post-correction coseismic offsets of

344   5 - 14 mm, while the rest show offsets less than 5 mm. Our MPOE correction method reduces the

345   conspicuous artificial offset present in the SBAS-based coseismic corrected time series (MPOE

346   produces 7 mm, while the SDOE coseismic correction produces 21 mm leftover offset), but does

347   not fully capture and remove it. We attribute this leftover coseismic displacements at these pixel

348   locations to the high noise levels present in the InSAR time series data, and in the Discussion

349   section we explore a further GNSS-based correction step that helps alleviate this issue (see

350   section 4.2).

351

352   In principle, when we remove the conspicuous coseismic displacements, the leftover earthquake-

353   related deformation is due to postseismic processes. Previous assessments of GNSS motions

354   have resulted in estimates of cumulative postseismic motion up to tens of millimeters near the

355   earthquake area (Brooks *et al.* 2020; Floyd *et al.* 2020), which are in reasonable agreement with

356   those measured by Wang & Bürgmann (2020) from InSAR measurements and by Golriz et al.

357   (2021) from high-rate GNSS displacements. Due to the relatively small amounts of postseismic

358   displacements over the scene, we choose to apply the CSS (Tymofyeyeva & Fialko, 2015)

359   correction to our coseismic-corrected time series. We seek to assess whether we achieve

360   reasonable results with this method, despite the fact that the surface is experiencing non-steady-

361   state motions. In order to reduce the noise level caused by atmospheric effects, we choose to run

362   these new coseismic-corrected time series through SBAS using a subjective temporal smoothing

363   factor of one and a three-iteration CSS correction (Tymofyeyeva & Fialko, 2015). The temporal

364   smoothing factor (Schmidt & Bürgmann, 2003) helps control large changes from epoch to epoch

365   in the time series (with a factor of zero providing no smoothing and a value of 10 for example,

366   causing strong smoothing), while the CSS correction helps correct for propagation delays

367   through the troposphere and the ionosphere using an iterative procedure (Tymofyeyeva & Fialko,

368   2015, see their Section 2; Xu *et al.* 2017). Multiple iterations are recommended for the CSS

369   correction to be most effective (Tymofyeyeva & Fialko, 2015), and we choose three iterations

370   here to balance computation time efficiency and effectiveness. Results of this processing are

371   presented in Fig. 4C.
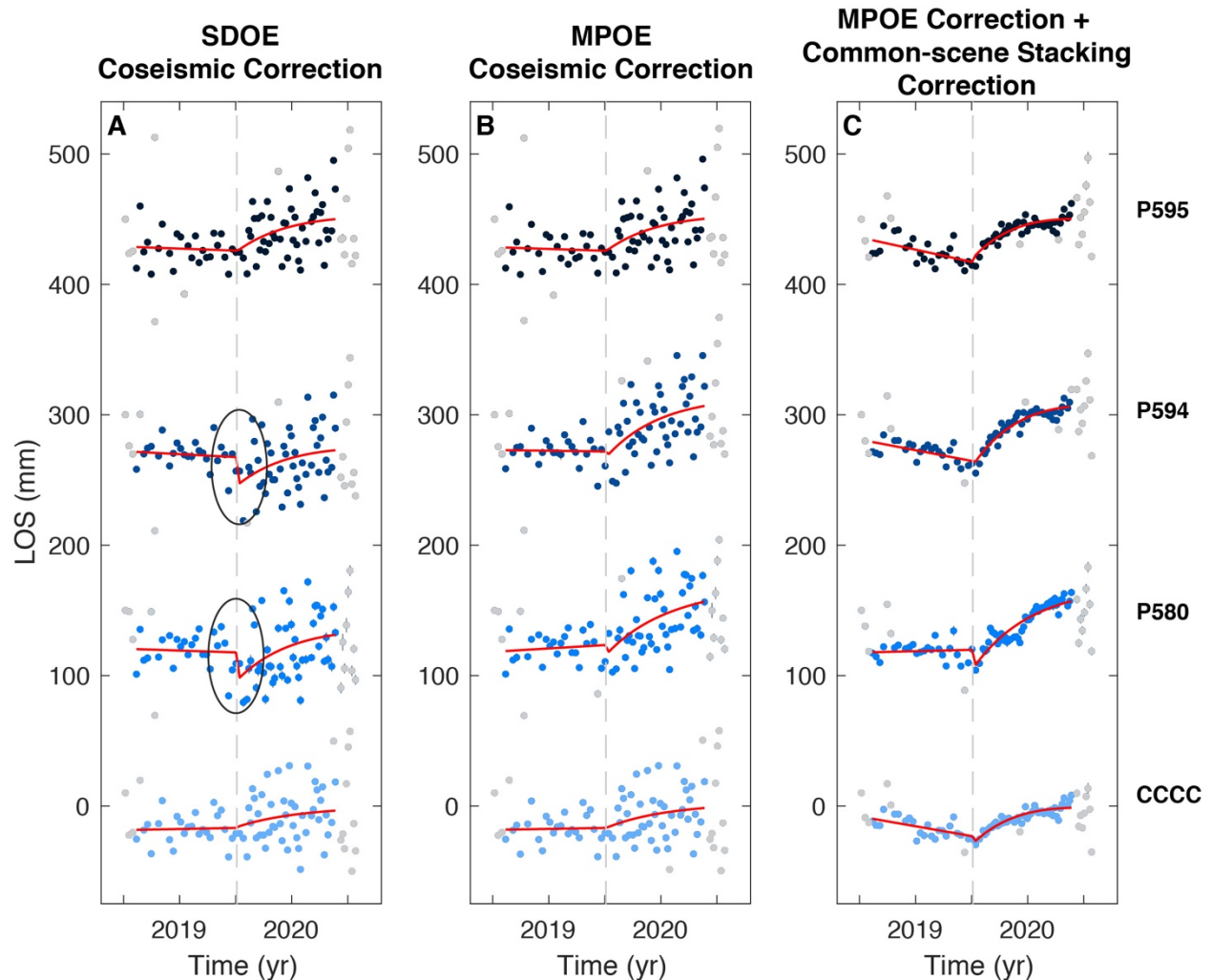
372

373   Figure 4. Results of our two coseismic correction methodologies on four pixels of our descending track

374   InSAR time series; (A) shows the Simple Difference Offset Estimate (SDOE) correction, (B) shows the

375   Multiparameter Offset Estimate (MPOE) correction, and (C) shows the MPOE correction in combination

376   with the CSS atmospheric correction. Red lines are the respective estimated time series models. Grey

377   points in the InSAR time series are points that have been removed before model estimation analysis.

378

379   For all our SBAS-produced InSAR time series, we trim off three points at the beginnings and

380   nine points at the ends of the time series data (Fig. 4). This is due to the fact that the CSS noise

381   estimate depends on having data on both sides of any given time epoch. Thus, at the beginning

382   and end of the series, there is not a lengthy enough dataset on the given side to achieve an

383   accurate result. We then apply a check for conspicuous outliers, using a 25-point (epoch) mean

15

384   moving window, which will reject points that are more than three standard deviations away from

385   the mean of a 25-point set. For a 6 - 12 day repeat time, this equates to a window of 72 - 300

386   days. We chose this window as it was the minimum one we tested that removed the most visually

387   conspicuous outliers in the time series. This generally removes up to 1 - 3 data points in each

388   time series. Once outliers and ends are removed, we estimate our time series model as described

389   in Section 2.4. In doing so, we estimate varying amounts of postseismic motion for different

390   stations over the first two months after the events, ranging from 3.9 - 14.3 mm for our coseismic-

391   corrected time series, and 3.5 - 24.3 mm for our coseismic-corrected and CSS-corrected time

392   series at GNSS station positions nearest to the event (Table 1). Plotted estimates of cumulative

393   postseismic deformation are presented as interpolated surfaces in Fig. 5 (a comparison between

394   the descending track and ascending track estimates is presented in Fig. S3).

395

396   The estimated postseismic displacements measured in our InSAR time series are in general much

397   larger than those measured with GNSS instruments (two to seven times larger for the stations

398   presented in Fig. 4). We further discuss, investigate, and reduce this discrepancy in the next

399   section.

400

401   Table 1. Estimated cumulative postseismic deformation in a 48-day period for ten GNSS station locations

402   in our InSAR time series datasets, as compared to that estimated from Wang & Bürgmann (2020).

Station	Location		Cumulative Postsiesmic (48 days)						Wang & Bürgmann (2020)	
			This Study†				GNSS-Cor** InSAR (CC)	GNSS-Cor** InSAR (CC+AC)		
	Longitude (°W)	Latitude (°N)	InSAR (CC)* (mm)	InSAR (CC+AC)* (mm)	GNSS* (mm)	GNSS ± 1σ (mm)	(mm)	(mm)	InSAR § (mm)	GNSS § (mm)
BEPK	-118.07409	35.87839	14.33	11.70	-2.33 ± 0.40	-1.22 ± 0.32	-2.67	-1.18	-	-
CCCC	-117.67117	35.56531	3.92	6.62	-0.71 ± 0.34	0.39 ± 0.28	0.64	0.54	~ 3.0	-3 — -4
GOL2	-116.88925	35.42516	8.07	3.55	1.35 ± 0.36	2.59 ± 0.31	2.22	1.22	-	-
ISLK	-118.47430	35.66227	13.66	24.31	-0.01 ± 0.46	0.80 ± 0.41	1.03	2.73	-	-
P569	-118.12377	35.37797	10.46	11.85	-0.36 ± 0.37	0.71 ± 0.34	1.39	0.78	-	-
P570	-118.26004	35.66735	10.56	19.87	-1.09 ± 0.34	0.08 ± 0.25	0.62	2.09	-	-
P580	-117.19223	35.62095	10.13	7.63	2.74 ± 0.28	3.72 ± 0.25	3.36	3.74	-	-

									12.5 -	
P594	-117.39013	35.89671	11.25	8.28	3.92 ± 0.57	6.14 ± 0.52	5.38	5.20	14	~ 4
P595	-117.40284	35.69756	7.62	7.01	2.51 ± 0.29	3.68 ± 0.26	3.86	3.14	~3.0	3 — 4
P597	-116.88840	35.71060	9.25	3.49	1.93 ± 0.30	2.99 ± 0.26	1.73	1.33	-	-

† Using an exponential function with a tau term of 0.5 yr (182.5 days)

* Time Series referenced to the location of station HCMN

CC = MPOE Coseismic Correction applied

AC = Common-scene Stacking Atmospheric Correction applied

** Elevation Dependent Atmospheric Correction applied

§ Values extracted from Wang & Bürgmann (2020) figure 7b

403
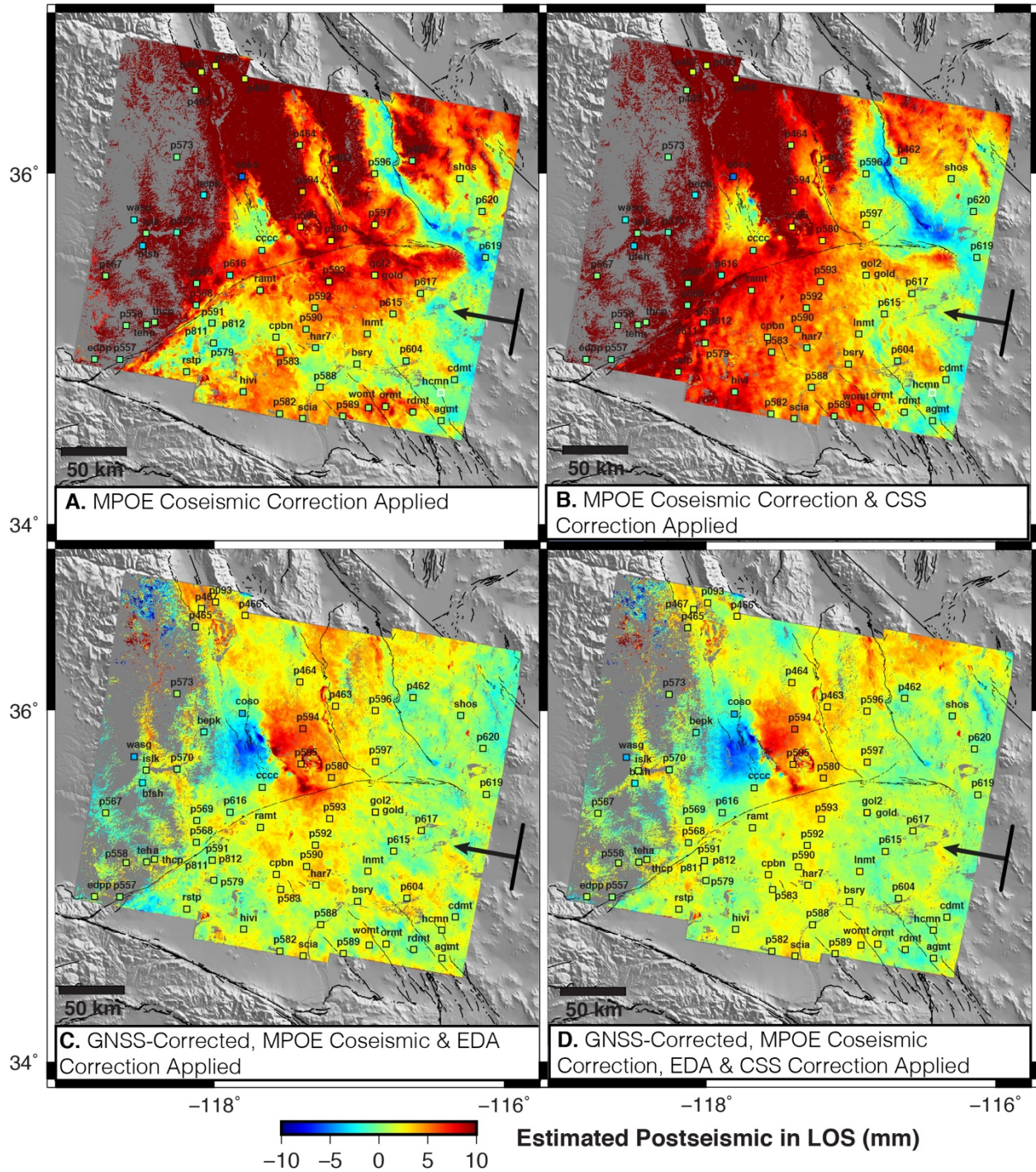
Figure 5. Postseismic displacements estimated from sets of InSAR time series for the 48-day period following the event (July 5th to August 21st); (A) Estimated from our coseismic corrected InSAR time series; (B) Estimated from our coseismic-corrected InSAR time series, with the additional Common-scene Stacking (CSS) correction, (C) Estimated from our GNSS-Corrected, Elevation Dependent Atmospheric (EDA) correction-corrected, coseismic-corrected InSAR time series, and (D) Estimated from the same GNSS- and EDA correction-corrected InSAR time series with the additional CSS correction. All labeled

411   squares show the magnitude of postseismic displacements estimated from the GNSS time series. White

412   outlined square in (A,B) is the reference point for non-GNSS-corrected InSAR time series (bottom right

413   of (A,B)), labeled HCMN.

414

415   3.1 Improved Isolation of the Postseismic Signal

416   In removing the coseismic offset from our InSAR time series, we have produced a dataset that

417   can undergo temporal smoothing and a CSS atmospheric correction within the SBAS program.

418   The discrepancy noted between estimates of postseismic deformation from our InSAR and

419   GNSS time series, however, motivates us to investigate how we can achieve more consistent

420   estimated results between these two datasets. Accurately estimating the magnitude of postseismic

421   deformation following a large earthquake is crucial given that these estimates inform modeling

422   efforts to piece apart mechanisms of postseismic deformation and determine possible stress-

423   based effects on nearby faults.

424

425   In theory, InSAR measurements of ground motion in the LOS direction should match the GNSS

426   measurements of ground motion projected into LOS, assuming that they are observing the same

427   processes at the surface, particularly earthquake related processes. If these measurements are a

428   poor match to each other, one of the main explanations is that InSAR is known to contain many

429   sources of noise, including spatially and temporally dependent tropospheric, ionospheric,

430   decorrelation and topographic effects, as well as processing-based phase unwrapping errors

431   (Chen & Zebker, 2014; Fattahi & Amelung, 2015; Liu *et al.* 2014; Zebker *et al.* 1997; Zebker &

432   Villasenor, 1992). GNSS motions, on the other hand, have many of these types of errors

433   accounted for and corrected during processing. Furthermore, GNSS measurements can provide

434   an "absolute" (global) reference system for InSAR measurements. Therefore, if we correct our

435   InSAR data using GNSS motions, we can achieve a more accurate integrated LOS time series

436   product (Neely *et al.* 2020; Xu *et al.* 2021). In the following section, we use this approach to

437   produce an integrated time series product that takes into account the Ridgecrest earthquake

438   offsets and provides an improved estimate of postseismic deformation.

439

440   3.1.1 Correcting InSAR with Continuous GNSS Motions

441   To correct our descending and ascending track InSAR interferograms using continuous GNSS

442   daily displacements, we first downsample our daily GNSS time series to a weekly format (Klein

443   *et al.* 2019) to suppress the scatters in daily solutions (considering the 6-day minimal repeat of

444   Sentinel-1). To do so, we apply a median filter on the weekly data to ensure only representative

445   motions are included. In the special case of the Ridgecrest earthquake sequence, which occurred

446   midweek, we break up a single week into "pre-Ridgecrest earthquake" and "post-Ridgecrest

447   earthquake" partial weeks of four and three days respectively, to ensure we do not smooth over

448   the coseismic displacements.

449

450   Once the GNSS weekly dataset is prepared, we begin by applying a combination of the

451   methodologies of Argus et al. (2005), Neely et al. (2020) and Xu et al. (2021). This GNSS-

452   correction process is described in detail in the methods section of Xu et al. (2021), and we

453   describe here how we deviate from their process. We begin by applying an Elevation Dependent

454   Atmospheric (EDA) phase correction to all non-Ridgecrest earthquake spanning interferograms,

455   in order to help correct for topographically correlated atmospheric path delays (Elliott *et al.*

456   2008). This assumes a linear relationship between path delay and height, which has been shown

457   by Elliott et al. (2008) to be a reasonable approximation. To start with, we do not apply the EDA

458   correction to the earthquake spanning interferograms due to the large amount of coseismic

459   deformation present in each interferogram. Once the EDA correction has been applied, we

460   calculate the GNSS displacements in LOS using all three GNSS components for all

461   interferogram pairs, and then calculate the residuals (InSAR - GNSS) between the InSAR and

462   GNSS displacements (See Fig. S4 for visual examples). A script that accomplishes this

463   correction is included in the most recent GMTSAR version 6.1 software distribution

464   (correct_insar_with_gnss.csh, GMTSAR GitHub: https://github.com/gmtsar/gmtsar). This

465   correction does not currently take GNSS uncertainties (in particular, larger vertical uncertainties)

466   into account. We then apply a Gaussian filter with a wavelength of 40 km, which is the average

467   distance between our GNSS stations, to the interpolated residual surface, and subtract that final

468   interpolated, filtered surface from the InSAR interferogram.

469

470   With our new set of GNSS-corrected interferograms, we apply SBAS to calculate our

471   deformation time series in the same way as before. First, we run SBAS with all interferograms

472 with no additional smoothing and no CSS correction. This set includes the Ridgecrest earthquake

473 offset (Fig. 6A; Fig. S5). We then calculate our MPOE coseismic correction grid, and remove it

474 from our ten earthquake-spanning GNSS-corrected interferograms. At this point, now that the

475 coseismic deformation is removed, we then apply the EDA correction to these specific

476 earthquake-spanning interferograms and run a second SBAS with no additional smoothing and

477 no CSS correction to assess the results of the coseismic correction (Fig. 6B; Fig. S6). Lastly, we

478 run a third SBAS that includes the CSS correction (Tymofyeyeva & Fialko, 2015) and a

479 temporal smoothing parameter (Schmidt & Bürgmann, 2003) to produce the final results

480 presented in Fig. 6C (Fig. S7). This newly created InSAR time series dataset more closely

481 matches the weekly GNSS time series observations. Fig. S8 illustrates the same effects for the

482 ascending InSAR time series dataset.

483
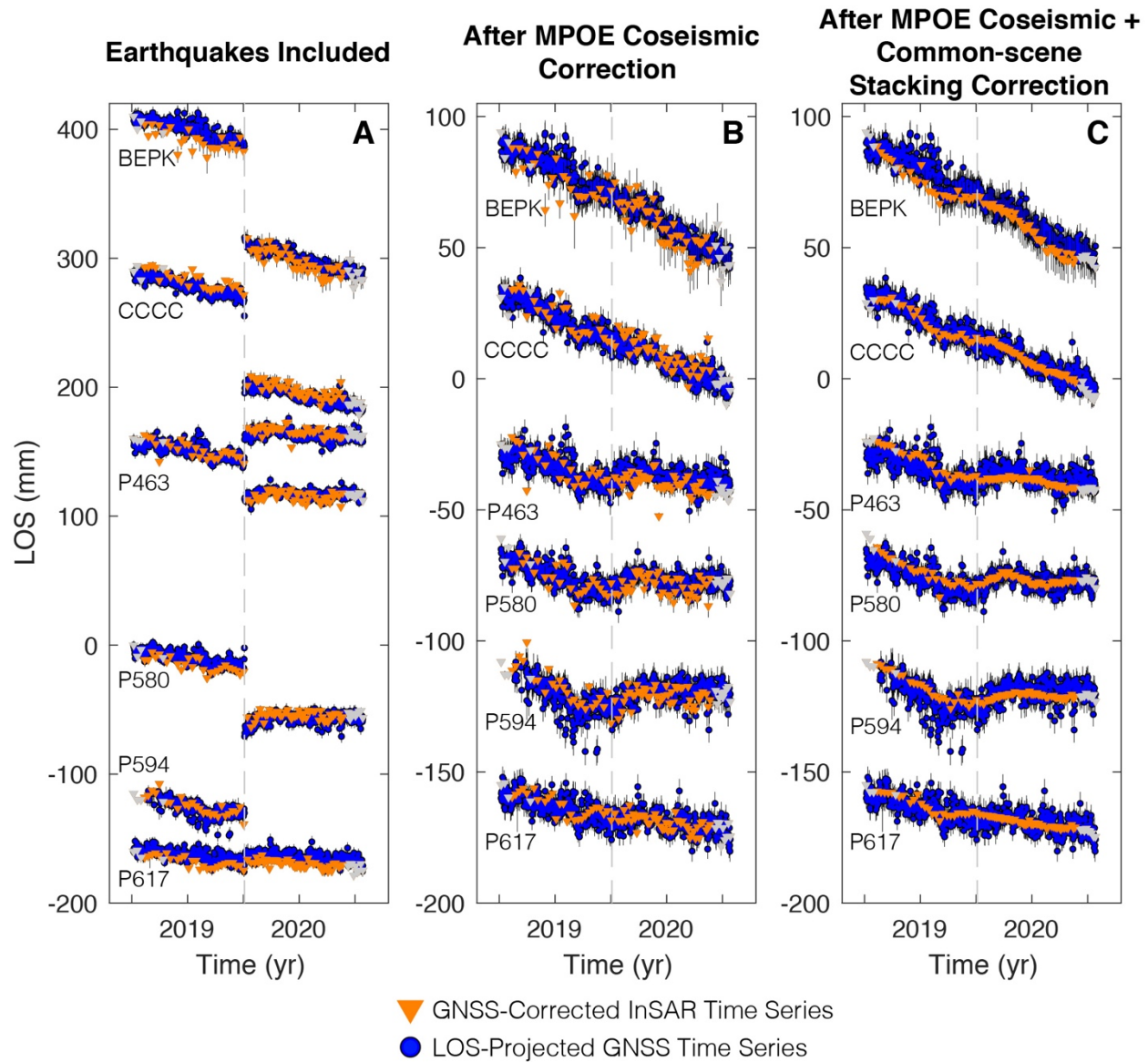
Figure 6. Descending track 71 GNSS-corrected InSAR time series plotted on top of GNSS time series in three cases; (A) Time series including the earthquakes' offset (with an Elevation Dependent Atmospheric (EDA) Correction applied to all but coseismic interferograms); (B) Results of applying our MPOE coseismic correction with an EDA correction for all interferograms and (C) Results of applying the CSS atmospheric correction. Note scale on panel A has a larger LOS range for display purposes. See Fig. S7 for the ascending track version.

3.2 Results of Postseismic Estimates from GNSS-Corrected InSAR Time Series

When we calculate estimated postseismic displacements from these GNSS-corrected and MPOE coseismic-corrected InSAR time series, we find that they match those estimated from GNSS time

495   series much more closely, with 82% of stations matching within 2σ uncertainties of GNSS

496   estimates (92% within 3σ uncertainties of GNSS estimates). The comparison of Fig. 5A and Fig.

497   5C visually illustrates the amount of improvement between postseismic estimates for a 48-day

498   period. In Fig. 5C, the background surface from our InSAR multiparameter estimate grid

499   matches the GNSS postseismic deformation estimates (plotted as squares) much better than the

500   postseismic surface estimated from our coseismic corrected InSAR time series that does not have

501   the GNSS or EDA correction (Fig. 5A), particularly on the western (far-range) side of the scene.

502   Table 1 presents the estimated values of postseismic displacement derived from InSAR time

503   series for ten station locations nearest to the earthquake event. Figure 7 illustrates a direct

504   scatterplot comparison for all 62 station locations' interseismic, coseismic and postseismic

505   estimates.

506

507   In addition, when we assess the performance of our MPOE coseismic correction on the

508   descending track GNSS-corrected time series, we find that any leftover estimated coseismic

509   displacement is < 2 mm, with only 11 stations presenting between >1 mm of displacement. This

510   indicates that the GNSS data-based correction reduces the levels of noise in the data, enabling us

511   to achieve a more accurate coseismic correction for all stations (Fig. 7B). In the ascending track,

512   only 15 of 64 stations show leftover estimated coseismic displacements that are > 2 mm, with all

513   but two of those stations exhibiting 2 - 4 mm of leftover displacement.

514
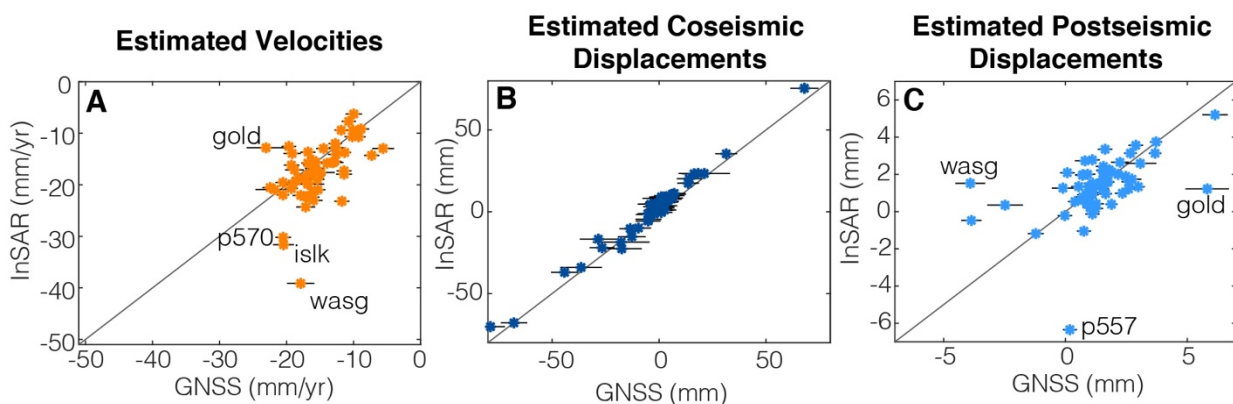
515

516   Figure 7. Scatterplot comparison of time series model parameters estimated from GNSS time series for 62

517   stations (plotted with their formal one-sigma uncertainties) and our descending track GNSS-corrected

518   InSAR time series for the same pixel locations, plotted on top of a line with a slope of one; (A) shows

519   estimated velocity values, (B) shows estimated coseismic displacements and (C) shows estimated

520 cumulative postseismic displacements for a 48-day period following the earthquake. We label the largest

521 outlier GNSS stations (see section 3.3.1 for discussion).

522

523 3.3 InSAR Time Series-derived Earthquake Cycle Products

524 An added benefit of calculating a MPOE coseismic estimate method is that we can also solve for

525 other time series parameters for every pixel across the InSAR scene, including both postseismic

526 displacements and interseismic velocity. This method produces Fig. 8, which illustrates the

527 multiparameter estimates of interseismic velocity, coseismic displacement and the amount of

528 cumulative postseismic displacements estimated over a 48-day period following the earthquake.

529

530
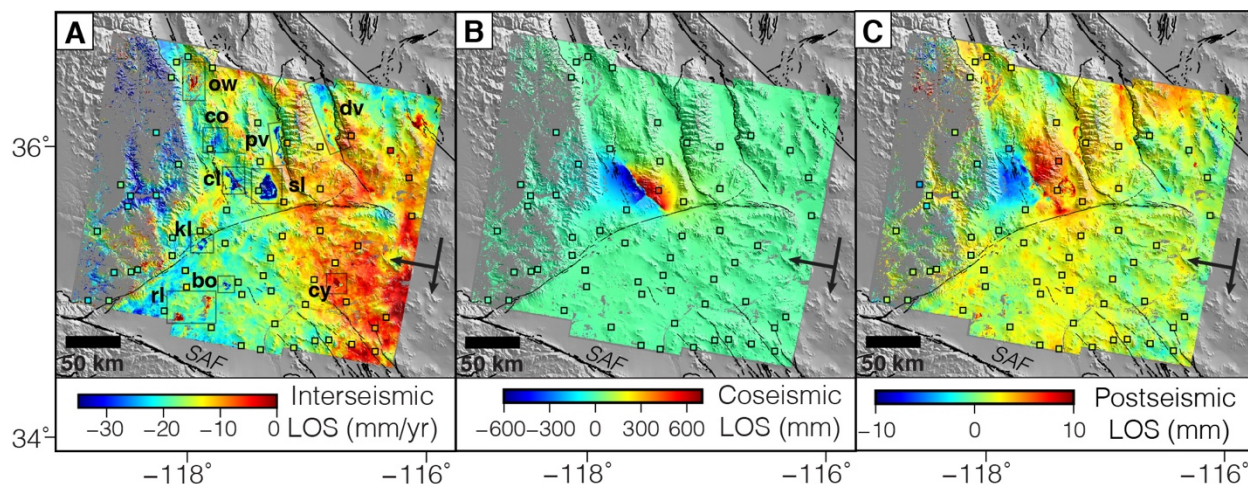
531 Figure 8. Estimated earthquake cycle grids derived from our GNSS-corrected, coseismic-corrected, EDA-

532 corrected and CSS-corrected InSAR time series, overlaid on topography, with areas <0.45 coherence

533 masked out; (A) shows the estimated interseismic velocity field with highlighted areas of subsidence or

534 uplift, (B) shows the estimated coseismic displacement and (C) shows the cumulative estimated

535 postseismic displacements for a 48-day period following the event (or $D_{postseismic}(t)$ in [3]). Squares are

536 locations of GNSS stations, with the equivalent values estimated from GNSS time series. Note changes in

537 scales between panels. Abbreviations are bo = Borax Mine, cl = China Lake, co = Coso Volcanic Field,

538 cy = Coyote dry lake, dv = Death Valley, kl = Koehn Lake, ow = Owens Lake, pv = Panamint Valley, rl =

539 Rosamund and Rodgers dry lakes, SAF = San Andreas Fault, and sl = Searles Lake.

540

541 In our two-year interseismic velocity estimate grid, we can see a gradient of surface motion away

542 from the satellite increasing towards the northwest. We also observe the effects of subsidence

543 occurring at Searles Lake (largest blue feature in center of Fig. 8A), China Lake (labeled box to

544 the northwest), Coso Volcanic field (box to the north), the dry lakebed in the southern Panamint

545 Valley near Ballarat (box to the northeast of Searles Lake), Koehn Lake (box located in the

546 stepover of the Garlock Fault to the southwest) and the Borax mining activity occurring north of

547 Boron, CA (small box labeled "bo"). In addition, we can see possible uplift around the desert

548 lakebeds of Rosamund dry lake, Rogers dry lake in the western Mojave, Coyote dry late in the

549 eastern Mojave, and Owens Lake near Lone Pine in the Owens Valley to the northwest. In Death

550 Valley, we can see signals of both uplift and subsidence in different areas of Badwater Basin.

551

552 Estimating 48 days of cumulative postseismic displacement with our multiparameter method

553 results in an image (Fig. 8C) that shows the expected postseismic motions with respect to the

554 descending satellite along both the M_W 6.4 and M_W 7.1 rupture zones, and highlights areas of

555 potential afterslip or poroelastic rebound along the M_W 7.1 rupture zone. Our estimated result

556 agrees fairly well with the descending track postseismic interferogram presented by Wang &

557 Bürgmann (2020) (see their Figure 7b) near the rupture area, and both identify the largest area of

558 postseismic slip to be near the epicenter of the M_W 7.1 event. Analysis of the exact mechanisms

559 of this postseismic deformation is beyond the scope of this study, but is an active area of research

560 (e.g., Wang *et al.* 2021).

561

562 By using a multiparameter method to estimate the postseismic amplitude from our full GNSS-

563 corrected InSAR time series, we can use this amplitude grid to calculate a cumulative

564 postseismic displacement grid over any given time period (Fig S9). To do this, one needs to

565 assume (1) the postseismic deformation from the event is best fit by a chosen postseismic

566 function (the one used to estimate the amplitude), and (2) the characteristic relaxation time (τ), is

567 constant over both time and space. These assumptions are not necessarily valid, given that best

568 fit tau relaxation times can vary across time (e.g., Jiang *et al.* 2021) and space (e.g., Sobrero *et*

569 *al.,* 2020), and different postseismic functions (with single or multiple terms) may be needed to

570 describe the full postseismic signals produced by an earthquake (e.g., afterslip, poroelastic

571 effects and/or viscoelastic relaxation, depending on the event). In the case of the Ridgecrest

572 event, we use an exponential function to describe the postseismic deformation as in [1] and [2]:

573

$$D_{postseismic}(t) = Amplitude * \left(1 - e^{-\frac{\Delta t}{\tau}}\right) \quad [3]$$

574

575

576 where amplitude is estimated during the least-squares inversion described in Section 2.3.2. In

577 using our chosen constant relaxation time tau = 0.5 year and an arbitrary 48-day time window

578 (Δt = 0.131 year), we can use the known, calculated grid of postseismic amplitude values to

579 calculate the cumulative postseismic displacements (Fig. 8C), as estimated from the InSAR time

580 series. This process allows us to calculate an InSAR-derived postseismic grid product for any

581 given postseismic time window after the earthquake (Fig. S9), as long as the above assumptions

582 are maintained. The earliest postseismic motions (e.g., Golriz *et al.* 2021) likely will be included

583 in the coseismic estimate from the InSAR data due to the unavoidable time constraint of the

584 twelve-day data collection window; however, addressing this issue is an active area of research.

585

586 3.3.1 A Note on Matching InSAR with GNSS

587 During our analysis of the descending GNSS-corrected InSAR time series, we observe that

588 stations ISLK, GOLD, P093, P465, P466, P467, P557, P558, P570, p620, SHOS, and WASG

589 produce InSAR time series that do not match the GNSS time series well (Fig. S10). In particular

590 their estimated long-term velocity trends exhibit a discrepancy of 7 - 33 mm/yr, depending on the

591 station. These stations either lie in areas of poor coherence or on the edges or corners of the

592 processed interferogram and therefore may have phase unwrapping errors or InSAR time series

593 that cannot be properly calculated through the SBAS process, without additional data on all sides

594 of the study area. Additionally, stations like GOLD and P557 have substantial (4-9 months-long)

595 gaps in their GNSS time series which can affect both the GNSS correction of the InSAR

596 interferograms, as well as the estimation of time series parameters. In many of these cases, we

597 expect that with longer time series these velocity trend mismatches will be reduced.

598

599 One difference between how we estimate time series model parameters between InSAR and

600 GNSS is that we choose not to estimate seasonal terms for our two-year GNSS-corrected InSAR

601 displacement time series model fits, as mentioned in section 2.3.2. This may introduce a source

602 of epistemic uncertainty when we then compare the results to GNSS time series models that have

603 had annual and semi-annual seasonal terms estimated. To illustrate the effect of not estimating

604 seasonal terms on our two-year InSAR time series, we plot six example location time series

605 residuals in Fig. S11, showing what the time series look like (Fig. 11A), what the residuals look

606   like without seasonal terms estimated (Fig. 11B) and what they look like with seasonal terms

607   estimated (Fig. 11C). To create this plot, we estimate an annual and semi-annual set of terms in

608   the same manner as we do for GNSS time series model fits (eqn. [1]). Seasonal signals can be

609   visually identified in our residuals, though we suggest that these signals are best recovered with a

610   longer span of time series than the two years we analyze here. In addition, we show what

611   differences occur in our interseismic and postseismic multiparameter estimate grids when

612   seasonal terms are estimated (Fig. S12). While there are no extreme differences, it appears as

613   though estimating seasonal terms increases the amplitude of the interseismic and postseismic

614   signals in certain areas across the scene, indicating that certain tradeoffs are occurring during the

615   time series inversions. More investigation, with a longer time series, is needed to best isolate the

616   postseismic signal from the other signals present in the time series.

617

618   4. Conclusion

619   The spatial resolution of InSAR displacement time series enables us to investigate many time-

620   dependent Earth processes in more detail than provided by individual interferogram pairs. When

621   using InSAR time series, however, common processing algorithms to reduce noise call for an

622   assumption of steady deformation through time, which becomes problematic when earthquakes

623   occur. In order to correct a sharp coseismic step introduced by an earthquake, we test two

624   methods that seek to remove the coseismic offset from InSAR time series: (1) a Simple

625   Difference Offset Estimate (SDOE) correction and (2) a Multiparameter Offset Estimate

626   (MPOE) time series inversion coseismic estimate correction. We apply these two methods to

627   time series surrounding the 2019 Ridgecrest earthquake sequence and find that the MPOE

628   coseismic correction more accurately corrects for coseismic displacements, as it can account for

629   noise present in the InSAR time series in a way that the SDOE correction cannot. Using this

630   correction produces an InSAR time series that can successfully undergo the application of

631   smoothing constraints as well as the CSS atmospheric correction.

632

633   To improve upon estimates of postseismic deformation from our InSAR time series, we employ

634   weekly GNSS displacement time series (Klein *et al.* 2019) to correct our interferograms (Neely

635   *et al.* 2020; Xu *et al.* 2021). Including LOS-projected GNSS displacements allows us to correct

636   for additional atmospheric signals in the interferogram and to provide an underlying frame of

637 reference for the InSAR interferograms. This results in GNSS-corrected InSAR interferograms
638 and time series, which produce more realistic estimates of postseismic deformation following the
639 Ridgecrest earthquake sequence than does our non-GNSS corrected InSAR time series. We
640 provide our two-year, GNSS-corrected, coseismic-corrected and EDA-corrected descending and
641 ascending track InSAR time series displacements for GNSS station locations near the Ridgecrest
642 earthquake (Data File S1, S2), as well as a set that have been corrected with the CSS correction
643 (Data File S3, S4).
644
645 The use of a multiparameter estimation approach also enables us to produce GNSS-corrected
646 InSAR data-derived estimates of interseismic, coseismic, and postseismic deformation, all in grid
647 format. We show that model-based postseismic deformation grids can be successfully estimated
648 from the InSAR time series for any time interval using an exponential postseismic model and a
649 multiparameter time series approach. Having an InSAR data-derived earthquake cycle product
650 will facilitate further characterization of the mechanisms of postseismic deformation following
651 the Ridgecrest event and help to discern which mechanisms (e.g., afterslip, poroelastic effects,
652 viscous relaxation) dominate.
653

662
663 6. Author Contribution Statement
664 K. Guns completed the InSAR time series processing and main analysis, with supervisory
665 assistance from both X. Xu and D. Sandwell. X. Xu and D. Sandwell wrote the main code for the
666 GNSS-correction processing. Y. Bock supervised the production of the GNSS displacement time
667 series and performed quality control with K. Guns. K. Guns completed the GNSS-correction

668 application processing, with supervisory assistance from X. Xu, D. Sandwell, and Y. Bock. K.

669 Guns wrote this paper with editorial and substantive changes from X. Xu, D. Sandwell, and Y.

670 Bock.

671

672 7. Data Availability Statement: All Sentinel-1 InSAR raw SLC data processed and presented in

673 this study are freely available from the Alaska Satellite Facility (https://search.asf.alaska.edu/#/)

674 and all GMTSAR processing programs and scripts are freely available on Github

675 (https://github.com/gmtsar/gmtsar). All processed GNSS data used in this study are freely

676 available on a weekly basis as explained at the Scripps Orbit and Permanent Array Center

677 (SOPAC) MEaSUREs products page (http://sopac-csrc.ucsd.edu/index.php/displacements/).

678

679 8. References
680 Agram, P.S., & Zebker H.A., 2009. Sparse Two-Dimensional Phase Unwrapping Using Regular-
681 Grid Methods, *IEEE Trans. Geosci. Remote Sens. Lett.*, 6(2), 327 - 331.
682 https://doi.org/10.1109/LGRS.2009.2012445 .

683

684 Argus D.F., Heflin, M.B., Peltzer, G., Crampé, F., & Webb, F.H., 2005. Interseismic strain
685 accumulation and anthropogenic motion in metropolitan Los Angeles, *Journal of Geophysical*
686 *Research*, 110, B04401. https://doi.org/10.1029/2003JB002934

687

688 Bekaert, D.P.S., Handwerger, A.L., Agram, P., & Kirschbaum, D.B., 2020. InSAR-based
689 detection method for mapping and monitoring slow-moving landslides in remote regions with
690 steep and mountainous terrain: An application to Nepal, *Remote Sensing of Environment,* 249.
691 https://doi.org/10.1016/j.rse.2020.111983

692

693 Berardino, P., Fornaro, G., Lanari, R., & Sansosti, E., 2002. A New Algorithm for Surface
694 Deformation Monitoring Based on Small Baseline Differential SAR Interferograms, *IEEE Trans.*
695 *Geosci. Remote Sens.*, 40, 11, 2375 -- 2383. https://doi.org/10.1109/TGRS.2002.803792

696

697 Biggs, J. & Wright, T.J., 2020. How satellite InSAR has grown from opportunistic science to
698 routine monitoring over the last decade, *Nature Communications*.
699 https://doi.org/10.1038/s41467-020-17587-6

700

701 Bevis, M. and Brown, A., 2014. Trajectory models and reference frames for crustal motion
702 geodesy, *Journal of Geodesy*, 88, 283 -- 311. https://doi.org/10.1007/s00190-013-0685-5

703

704 Bock, Y. & Melgar, D., 2016. Physical Applications of GPS Geodesy: A Review, *Rep. Prog.*
705 *Phys*. 79, 10. https://doi.org/10.1088/0034-4885/79/10/106801

706

707 Bock, Y. & Wdowinski, S., 2021. GNSS Geodesy in Geophysics, Natural Hazards, Climate, and
708 the Environment, in Position, Navigation, and Timing Technologies in the 21st Century:

709   Integrated Satellite Navigation, Sensor Systems, and Civil Applications, *IEEE Trans. Geosci.*
710   *Remote Sens.*, 2021, 741 -- 820. https://doi.org/10.1002/9781119458449.ch28

712   Bock, Y., Fang, P., Knox, A., Sullivan, A., Jiang, S., Moore, A., Argus, D., Liu, Z., & Kedar, S.,
713   2021. Extended Solid Earth Science ESDR System Algorithm Theoretical Basis Document
714   (ATBD), October 11, 2021 MEaSUREs ROSES-17, April 4.
715   http://garner.ucsd.edu/pub/measuresESESES_products/ATBD/ESESES-ATBD.pdf

717   Brooks, B.A., Murray, J., Svarc, J., Phillips, E., Turner, R., Murray, M., Ericksen, T., Wang, K.,
718   Minson, S., Bürgmann, R., Pollitz, F., Hudnut, K., Nevitt, J., Roeloffs, E., Hernandez, J., &
719   Olson, B., 2020. Rapid Geodetic Observations of Spatiotemporally Varying Postseismic
720   Deformation Following the Ridgecrest Earthquake Sequence: The U.S., Geological Survey
721   Response, *Seismol. Res. Lett.*, 91, 2108 -- 2123. https://doi.org/10.1785/0220200007

723   Bürgmann, R., Rosen, P., & Fielding, E., 2000. Synthetic Aperture Radar interferometry to
724   measure Earth's surface topography and its deformation, Ann. Rev. Earth. planet. Sci., 28, 169 –
725   209, https://doi.org/10.1146/annurev.earth.28.1.169

727   Bürgmann, R. Hilley, G., Ferretti, A., & Novali, F., 2005. Resolving vertical tectonics in the San
728   Francisco Bay Area from permanent scatterer InSAR and GPS analysis, *Geology*, 34(3), 221-
729   224, https://doi.org/10.1130/G22064.1

731   Bürgmann, R., & Thatcher, W., 2013. Space geodesy: A revolution in crustal deformation
732   measurements of tectonic processes, *Geological Society of America Special Paper 500*, 1 -- 34.
733   https://doi.org/10.1130/2013.2500(12)

735   Chaussard, E., Wdowinski, S., Cabral-Cano, E., & Amelung, F., 2014. Land subsidence in
736   central Mexico detected by ALOS InSAR time-series, *Remote Sensing of Environment*, 140, 94 -
737   - 106. https://doi.org/10.1016/j.rse.2013.08.038

739   Chen, C.W., & Zebker, H.A., 2002. Phase Unwrapping for Large SAR Interferograms: Statistical
740   Segmentation and Generalized Network Models, *IEEE Trans. Geosci. Remote Sens.*, 40(8), 1709
741   -- 1719. https://doi.org/10.1109/TGRS.2002.802453

743   Chen, C.C., & Zebker, H.A., 2014. Reducing Ionospheric Effects in InSAR Data Using Accurate
744   Coregistration, *IEEE Trans. Geosci. Remote Sens.*, 52(1), 60 -- 70.
745   https://doi.org/10.1109/TGRS.2012.2236098

747   Dixon, T., Amelung, F., Ferretti, A., Novali, F., Rocca, F., Dokka, R., Sella, G., Kim, S.-W.,
748   Wdowinski, S., & Whitman, D., 2006. Subsidence and flooding in New Orleans, Nature, 441,
749   587-588, https://doi.org/10.1038/441587a

751   Elliott, J.R., Biggs, J., Parsons, B., & Wright, T.J., 2008. InSAR slip rate determination on the
752   Altyn Tagh Fault, northern Tibet, in the presence of topographically correlated atmospheric
753   delays, *Geophys. Res. Lett.*, 35. https://doi.org/10.1029/2008GL033659
754

755   Fattahi, H., & Amelung, F., 2015. InSAR bias and uncertainty due to the systematic and
756   stochastic tropospheric delay, *J. Geophys. Res. Solid Earth*, 120, 8758 -- 8773.
757   https://doi.org/10.1002/2015JB012419
758
759   Fattahi, H., & Amelung, F., 2016. InSAR observations of strain accumulation and fault creep
760   along the Chaman Fault system, Pakistan and Afghanistan. *Geophys. Res. Let.*, 43(16), 8399-
761   8406. https://doi.org/10.1002/2016GL070121
762
763   Floyd, M., Funning, G., Fialko, Y., Terry, R., & Herring, T., 2020. Survey and Continuous
764   GNSS in the Vicinity of the July 2019 Ridgecrest Earthquakes, *Seismol. Res. Lett.*, 91 (4): 2047–
765   2054. https://doi.org/10.1785/0220190324
766
767   Golriz, D, Bock, Y. & Xu, X., 2021. Defining the Coseismic Phase of the Crustal Deformation
768   Cycle with Seismogeodesy, *J. Geophys. Res. Solid Earth*, 126(10), e2021JB022002,
769   https://doi.org/10.1029/2021JB022002
770
771   Grandin, R., Vallée, M., Lacassin, R., 2017. Rupture process of the M_w 5.8 Pawnee, Oklahoma,
772   earthquake from Sentine11 InSAR and seismological data, *Seismol. Res. Lett.*, 88, 11.
773
774   Handwerger, A.L., Huang, M.-H., Fielding, E.J., Booth, A.M., & Bürgmann, R., 2019. A shift
775   from drought to extreme rainfall drives a stable landslide to catastrophic failure, *Nature Scientific*
776   *Reports*. https://doi.org/10.1038/s41598-018-38300-0
777
778   Hardebeck, J., 2020. A Stress-Similarity Triggering Model for Aftershocks of the M_W 6.4 and
779   7.1 Ridgecrest Earthquakes, *Bull. Seismol. Soc. Am.*, 110, 1716 -- 1727.
780   https://doi.org/10.1785/0120200015
781
782   Hetland, E.A., Musé, P., Simons, M., Lin, Y.N., Agram, P.S., & DiCaprio, C.J., 2012. Multiscale
783   InSAR Time Series (MInTS) analysis of surface deformation, *J. Geophys. Res.*,117, B02404.
784   https://doi.org/10.1029/2011JB008731
785
786   Hilley, G.E., Bürgman, R., Ferretti, A., Novali, F., & Rocca, F., 2004. Dynamics of Slow-
787   moving Landslides from Permanent Scatter Analysis, *Science*, 304(5679), 1952-1955,
788   https://doi.org/10.1126/science.1098821
789
790   Hooper, A., Bekaert, D., Spaans, K., & Ar1kan, M., 2012. Recent advances in SAR
791   interferometry time series analysis for measuring crustal deformation, *Tectonophysics*, 514-517,
792   https://doi.org/10.1016/j.tecto.2011.10.013
793
794   Hu, X., Bürgmann, R., Schulz, W. H., & Fielding, E. J., 2020. Four-dimensional surface motions
795   of the Slumgullion landslide and quantification of hydrometeorological forcing. *Nature*
796   *Communications*, 11(1), 1-9. https://doi.org/10.1038/s41467-020-16617-7
797
798   Hussain, E., Wright, T.J., Walters, R.J., Bekaert, D., Hooper, A., & Houseman, G.A., 2016.
799   Geodetic observations of postseismic creep in the decade after the 1999 Izmit earthquake,

800   Turkey: Implications for a shallow slip deficit, *J. Geophys. Res. Solid Earth*, 121, 2980 -- 3001.
801   https://doi.org/10.1002/2015JB012737
802
803   Jiang, J., Bock, Y., & Klein, E., 2021. Coevolving early afterslip and aftershock signatures of a
804   San Andreas fault rupture, *Sci. Adv.*, 7(15). https://doi.org/10.1126/sciadv.abc1606
805
806   Jin, Z., & Fialko, Y., 2020. Finite Slip Models of the 2019 Ridgecrest Earthquake Sequence
807   Constrained by Space Geodetic Data and Aftershock Locations, *Bull. Seismol. Soc. Am.*, 110,
808   1660 -- 1679. https://doi.org/10.1785/0120200060
809
810   Klein, E., Bock, Y., Xu, X., Sandwell, D.T., Golriz, D., Fang, P., & Su, L., 2019. Transient
811   Deformation in California from Two Decades of GPS Displacements: Implications for a Three-
812   Dimensional Kinematic Reference Frame, *J. Geophys. Res. Solid Earth*, 124.
813   https://doi.org/10.1029/2018JB017201
814
815   Liu, F., Elliott, J. R., Craig, T. J., Hooper, A., & Wright, T. J., 2021. Improving the Resolving
816   Power of InSAR for Earthquakes Using Time Series: A Case Study in Iran. *Geophys. Res. Let.*,
817   48(14), e2021GL093043. https://doi.org/10.1029/2021GL093043
818
819   Liu, Z., Jung, H.-S., & Lu, Z., 2014. Joint Correction of Ionosphere Noise and Orbital Error in L-
820   Band SAR Interferometry of Interseismic Deformation in Southern California, *IEEE Trans.*
821   *Geosci. Remote Sens.*, 52(6), 3421 -- 3427. https://doi.org/10.1109/TGRS.2013.227.2791
822
823   Milliner, C., Donnellan, A., Aati, S., Avouac, J. P., Zinke, R., Dolan, J. F., ... & Bürgmann, R.,
824   2021. Bookshelf Kinematics and the Effect of Dilatation on Fault Zone Inelastic Deformation:
825   Examples From Optical Image Correlation Measurements of the 2019 Ridgecrest Earthquake
826   Sequence. *J. Geophys. Res.: Solid Earth*, 126(3), e2020JB020551.
827   https://doi.org/10.1029/2020JB020551
828
829   Neely, W.R., Borsa, A.A., & Silverii, F., 2020. GInSAR: A cGPS Correction for Enhanced
830   InSAR Time Series. *IEEE Trans. Geosci. Remote Sens.*, 58(1).
831   https://doi.org/10.1109/TGRS.2019.2934118
832
833   Neely, W., Borsa, A.A., Burney, J.A., Levy, M.C., Silverii, F., & Sneed, M., 2021.
834   Characterization of Groundwater Recharge and Flow in California's San Joaquin Valley From
835   InSAR-Observed Surface Deformation, *Water Resources Research*, 57, e2020WR028451.
836   https://doi.org/10.1029/2020WR028451
837
838   Nikolaidis, R., 2002. Observation of geodetic and seismic deformation with the Global
839   Positioning System, PhD Dissertation, University of California, San Diego, La Jolla, California,
840   265 pgs.
841
842   Plesch, A., Shaw, J.H., Ross, Z.E., & Hauksson, E., 2020. Detailed 3D Fault Representations for
843   the 2019 Ridgecrest, California, Earthquake Sequence, *Bull. Seismol. Soc. Am.*, 110, 1818 --
844   1831. https://doi.org/10.1785/0120200053
845

846 Poland, M., Bürgmann, R., Dzurisin, D., Lisowski, M., Masterlark, T., Owen, S., & Fink, J.,
847 2006. Constraints on the mechanism of long-term steady subsidence at Medicine Lake volcano,
848 northern California, from GPS, leveling, and InSAR, *J. Volcanology and Geothermal Res.*, 150,
849 55 -78, https://10.1016/j.volgeores.2005.07.007

851 Ponti, D.J., Blair, J.L., Rosa, C.M., Thomas, K., Pickering, A.J., Dawson, T.E., 2020. Digital
852 datasets documenting surface fault rupture and ground deformation features produced by the
853 Ridgecrest M6.4 and M7.1 earthquake sequence of July 4 and 5, 2019, U.S. Geological Survey
854 data release, https://doi.org/10.5066/P9BZ5IJ9

856 Ross, Z.E., Idini, B., Jia, Z., Stephenson, O.L., Zhong, M., Wang, X., Zhan, Z., Simons, M.,
857 Fielding, E.J., Yun, S.-H., Hauksson, E., Moore, A.W., Liu, Z., & Jung, J., 2019. Hierarchical
858 interlocked orthogonal faulting in the 2019 Ridgecrest earthquake sequence, *Science*, 366, 346 --
859 351. https://doi.org/10.1126/science.aaz0109

861 Sandwell, D. T., Xu, X., Mellors, R., Wei, M., Tong, X., and Wessel, P., 2016. GMTSAR: An
862 InSAR Processing System Based on Generic Mapping Tools, Second Ed., available at
863 http://topex.ucsd.edu/gmtsar/tar/GMTSAR_2ND_TEX.pdf

865 Schmidt, D.A., & Bürgmann, R., 2003. Time-dependent land uplift and subsidence in the Santa
866 Clara valley, California, from a large interferometric synthetic aperture radar data set, *J.
867 Geophys. Res.*, 108(B9). https://doi.org/10.1029/2002JB002267

869 Shirzaei, M., & Bürgmann, R., 2013. Time-dependent model of creep on the Hayward fault from
870 joint inversion of 18 years of InSAR and surface creep data. *J. Geophys. Res.: Solid Earth*,
871 118(4), 1733-1746. https://doi.org/10.1002/jgrb.50149

873 Sobrero, F.S., Bevis, M., Gómez, D.D., & Wang, F., 2020. Logarithmic and exponential
874 transients in GNSS trajectory models as indicators of dominant processes in postseismic
875 deformation, *J. Geodesy*. https://doi.org/10.1007/s00190-020-01413-4

876 Tong, X., D. T. Sandwell, and B. Smith-Konter, 2013. High-resolution interseismic velocity data
877 along the San Andreas Fault from GPS and InSAR, *J. Geophys. Res.: Solid Earth*, 118.
878 https://doi.org/10.1029/2012JB009442

879 Tong, X. & Schmidt, D., 2016. Active movement of the Cascade landslide complex in
880 Washington from a coherence-based InSAR time series method, *Remote Sensing Environment*,
881 186. https://doi.org/10.1016/j.rse.2016.09.008

883 Tymofyeyeva, E. & Fialko, Y., 2015. Mitigation of atmospheric phase delays in InSAR data,
884 with application to the eastern California shear zone, *J. Geophys. Res. Solid Earth*, 120, 5952 --
885 5963. https://doi.org/10.1002/2015JB011886

887 Tymofyeyeva, E., Fialko, Y., Jiang, J., Xu, X., Sandwell, D., Bilham, R., ... & Moafipoor, S,
888 2019. Slow slip event on the southern San Andreas Fault triggered by the 2017 Mw 8.2 Chiapas
889 (Mexico) earthquake. *J. Geophys. Res.: Solid Earth*, 124(9), 9956-9975.
890 https://doi.org/10.1029/2018JB016765

891

892 Wang, K. & Bürgmann, R., 2020. Co- and Early Postseismic Deformation Due to the 2019
893 Ridgecrest Earthquake Sequence Constrained by Sentinel-1 and COSMO-SkyMed SAR Data,
894 *Seismol. Res. Lett.*, 91(4), 1998–2009. https://doi.org/10.1785/0220190299

895

896 Wang, K., Bürgamnn, R., Brooks, B., Svarc, J., Liu, Z., & Fielding, E., 2021. Modeling of
897 postseismic deformation following the 2019 Ridgecrest earthquake sequence, Abstract MR31A-
898 08 presented at 2021 American Geophysical Union Fall Meeting, New Orleans, LA and Online,
899 13-17 Dec.

900

901 Wei, S., Fielding, E., Leprince, S., Sladen, A., Avouac, J.-P., Helmberger, D., Hauksson, E.,
902 Chu, R., Simons, M., Hudnut, K., Herring, T., & Briggs, R., 2011. Superficial simplicity of the
903 2010 El Mayor-Cucapah earthquake of Baja California in Mexico, *Nature Geoscience*, 4, 615 --
904 618. https://doi.org/10.1038/NGEO1213

905

906 Weiss J.R., Walters, R.J., Morishita, Y., Wright, T.J., Lazecky, M., Wang, H., Hussain, E.,
907 Hooper, A.J., Elliott, J.R., Rollins, C., Yu, C., González, P.J., Spaans, K., Li, Z., & Parsons, B.,
908 2020. High-Resolution Surface Velocities and Strain for Anatonia From Sentinel-1 InSAR and
909 GNSS Data, *Geophy. Res. Lett.*, 47. https://doi.org/10.1029/2020GL087376

910

911 Xu, X., Sandwell, D.T., Tymofyeyeva, E., González-Ortega, A., & Tong, X., 2017. Tectonic and
912 Anthropogenic Deformation at the Cerro Prieto Geothermal Step-Over Revealed by Sentinel-1A
913 InSAR, *IEEE Trans. Geosci. Remote Sens.*, 55(9), 5284 -- 5292.
914 https://doi.org/10.1109/TGRS.2017.2704593

915

916 Xu, X., Ward, L. A., Jiang, J., Smith-Konter, B., Tymofyeyeva, E., Lindsey, E. O., ... &
917 Sandwell, D. T, 2018. Surface creep rate of the southern San Andreas fault modulated by stress
918 perturbations from nearby large events. *Geophys. Res. Let.*, 45(19), 10,259-10,268.
919 https://doi.org/10.1029/2018GL080137

920

921 Xu, X., Sandwell, D. T., & Smith-Konter, B., 2020b. Coseismic displacements and surface
922 fractures from Sentinel-1 InSAR: 2019 Ridgecrest earthquakes. *Seis. Res. Let.*, 91(4), 1979-1985.
923 https://doi.org/10.1785/0220190275

924

925 Xu, X., Sandwell, D.T., Ward, L.A., Milliner, C.W.D, Smith-Konter, B.R., Fang, P., & Bock, Y.,
926 2020a. Surface deformation associated with fractures near the 2019 Ridgecrest earthquake
927 sequence, *Science*, 370, 605 -- 608. https://doi.org/10.1126/science.abd1690

928

929 Xu, X., Sandwell, D.T., Klein, E., and Bock, Y., 2021. Integrated Sentinel-1 InSAR and GNSS
930 time-series along the San Andreas fault system, *J. Geophys. Res. Solid Earth*, 126(11),
931 e2021JB022579, https://doi.org/10.1029/2021JB022579

932

933 Zebker, H.A., & Villasenor, J., 1992. Decorrelation in interferometric radar echoes, *IEEE Trans.
934 Geosci. Remote Sens.*, *30*(5), 950-959.

935

936   Zebker, H.A., Rosen, P.A., & Hensley, S., 1997. Atmospheric effects in interferometric synthetic
937   aperture radar surface deformation and topographic maps, *J. Geophys. Res.*, 102(B4), 7547 --
938   7563.
939
940

Supplementary Files for:

GNSS-corrected InSAR Displacement Time Series Spanning the 2019 Ridgecrest, CA Earthquake

Katherine Guns[1†], Xiaohua Xu[2], Yehuda Bock[1], and David Sandwell[1]

[1]Institute of Geophysics and Planetary Physics, Scripps Institution of Oceanography, University of California, San Diego, La Jolla, CA, 92093-0225

[2]Institute for Geophysics, University of Texas at Austin, Austin, TX, 78758

[†]Corresponding Author: Katherine Guns kguns@ucsd.edu

Table of Contents

1. **Supplementary Figures**

2. **Supplementary Data Files**

Supplementary Figures
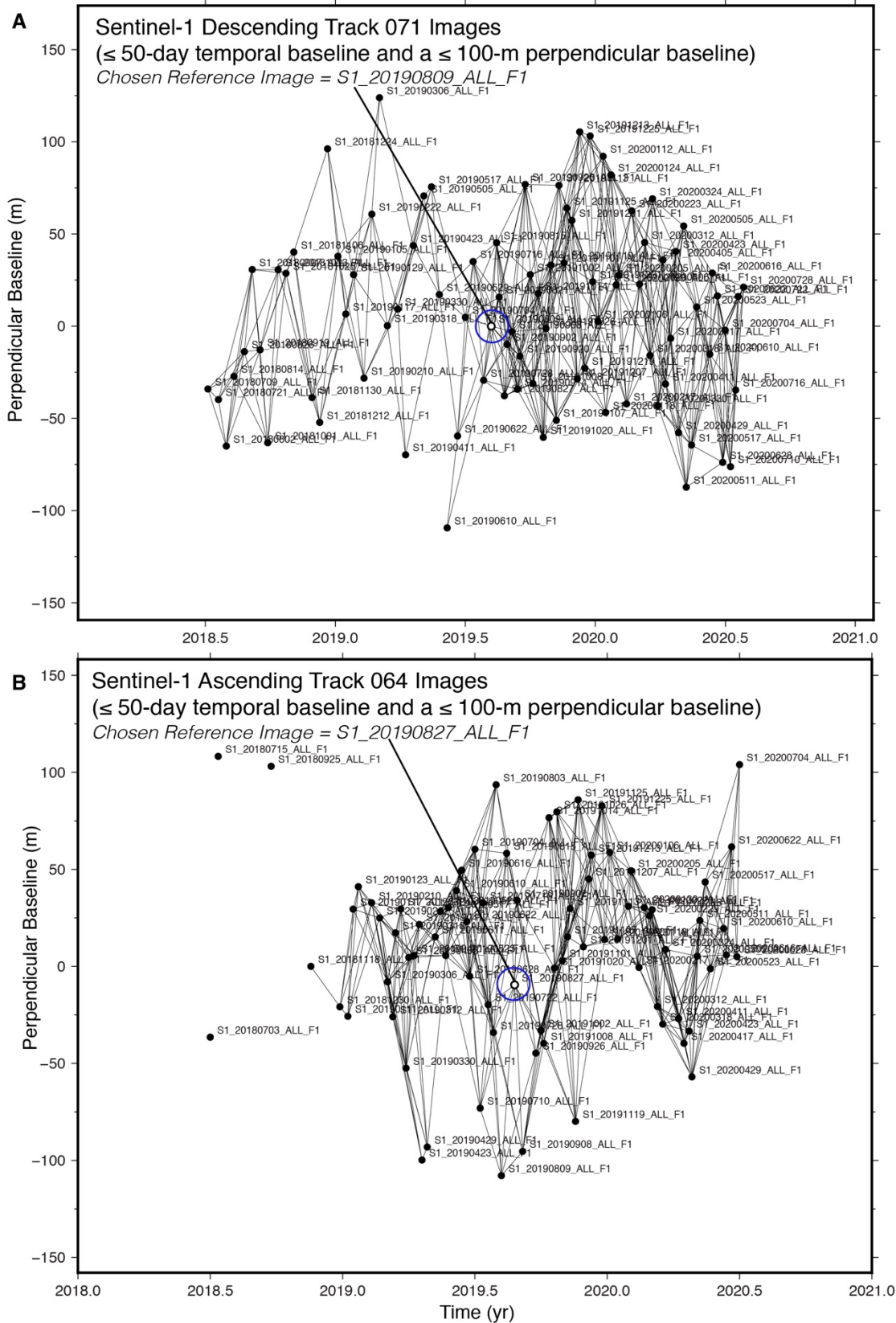
Figure S1. Plots of perpendicular baseline versus time for (A) the images used from Sentinel-1 Descending track 071 and (B) the images used from Sentinel-1 Ascending track 064. The images marked with blue circle are the chosen reference images for each track.
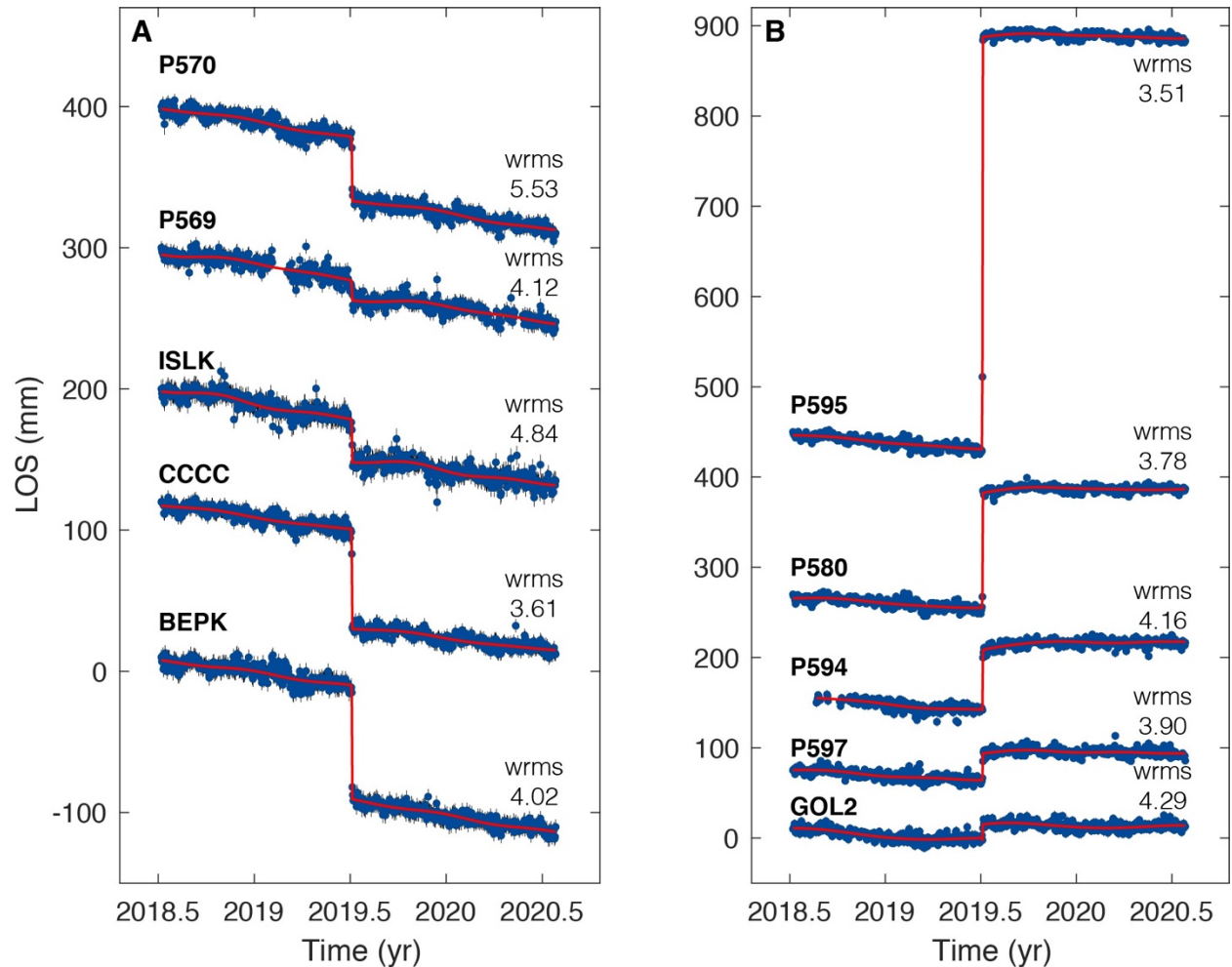
Figure S2. GNSS stacked time series projected in LOS, plotted with modeled motions (red lines) estimated through a weighted least squares inversion (A) shows stations that observed a negative coseismic displacement (away from the satellite) and (B) shows stations that observed a positive coseismic displacement (towards the satellite).
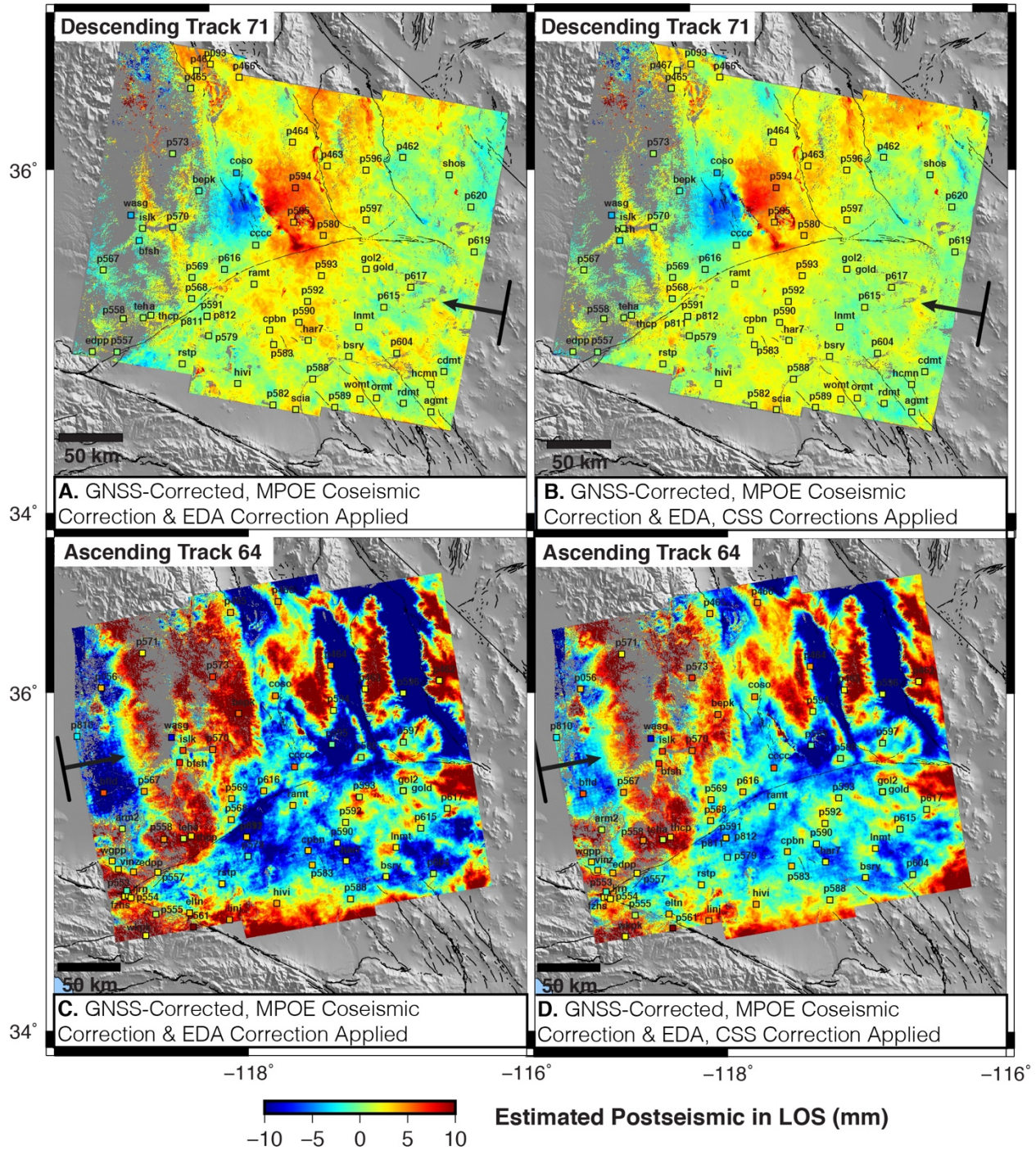
Figure S3. Comparison of MPOE-corrected estimates of 48 days of cumulative postseismic displacement between descending track 71 (A,B) and ascending track 64 (C,D) (Elevation Dependent Atmospheric (EDA) correction applied to all interferograms); (B) and (D) show the effect of the common scene stacking (CSS) atmospheric correction. Plotted squares illustrate the estimated 48 cumulative postseismic displacements from GNSS time series at stations across the scene for comparison.
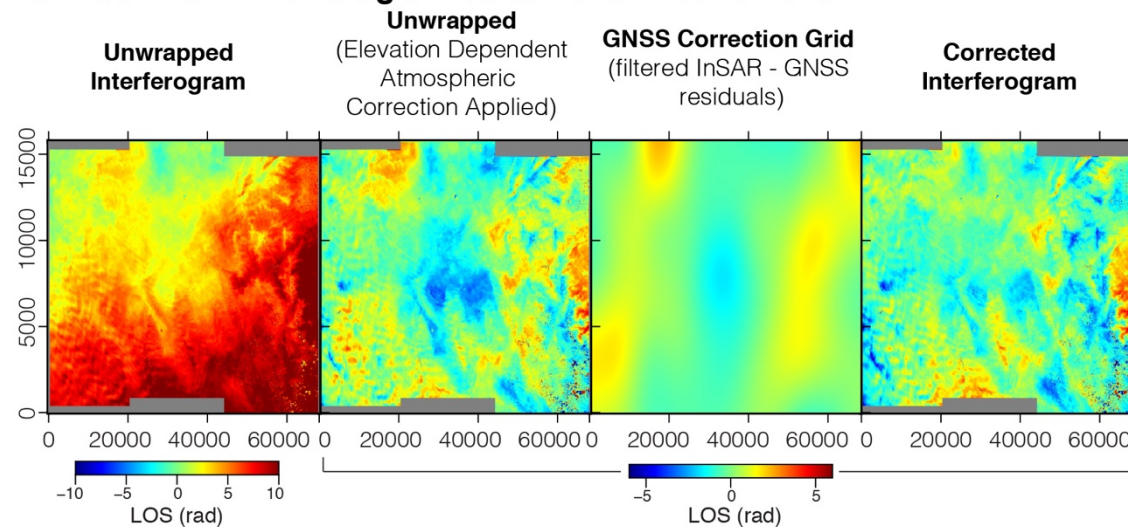
A. Track D071 Interferogram 03/18/2019 — 04/10/2019

Unwrapped Interferogram

Unwrapped (Elevation Dependent Atmospheric Correction Applied)

GNSS Correction Grid (filtered InSAR - GNSS residuals)

Corrected Interferogram

LOS (rad)

LOS (rad)
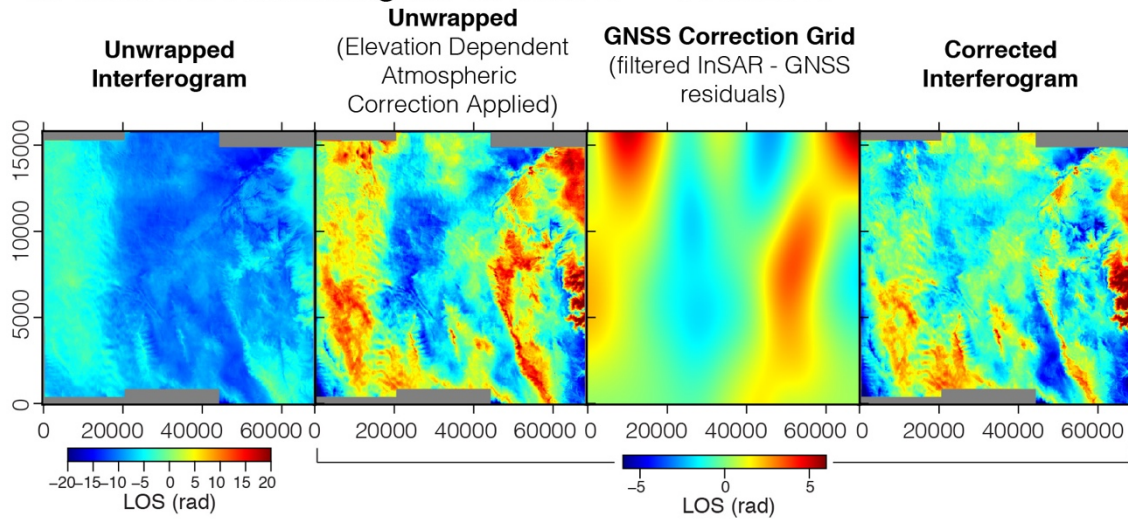
B. Track D071 Interferogram 07/04/2019 — 07/16/2019

Unwrapped Interferogram

(Elevation Dependent Atmospheric Correction Applied to Coseismic Interferograms after MPOE correction and GNSS-correction)

GNSS Correction Grid (filtered InSAR - GNSS residuals)

Corrected Interferogram

LOS (rad)

LOS (rad)

LOS (rad)
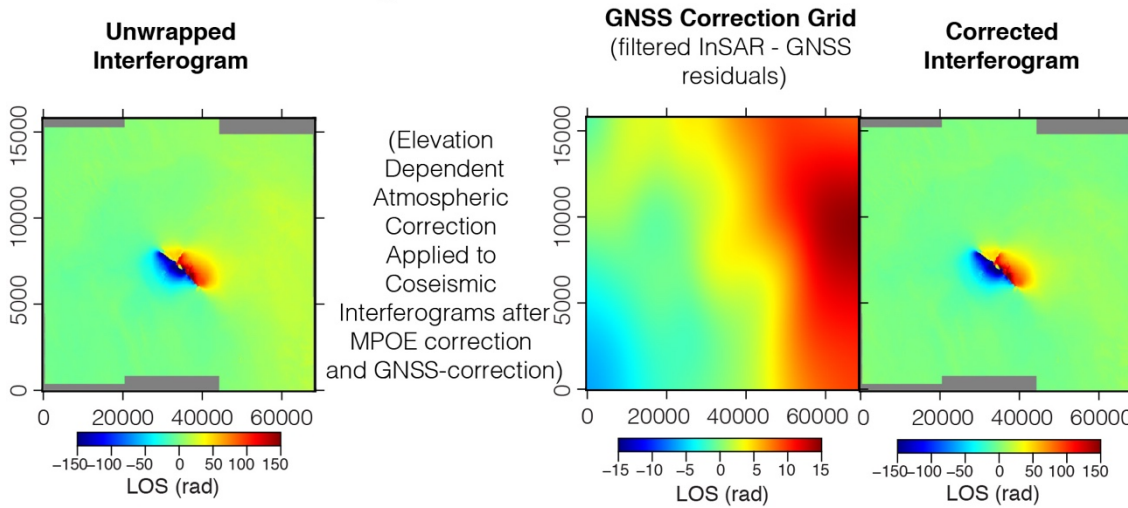
C. Track D071 Interferogram 08/08/2019 — 08/20/2019

Unwrapped Interferogram

Unwrapped (Elevation Dependent Atmospheric Correction Applied)

GNSS Correction Grid (filtered InSAR - GNSS residuals)

Corrected Interferogram

LOS (rad)

LOS (rad)

5

Figure S4. Three examples of our GNSS correction method, showing each stage of the correction process, including, from right to left the unwrapped interferogram, the post-Elevation Depended Atmospheric (EDA) phase correction-unwrapped interferogram, the GNSS correction grid, and the final corrected unwrapped interferogram, with both the elevation dependent correction and the GNSS correction applied; (A) shows an interferogram in late March to early April, (B) shows our first coseismic interferogram in July 2019, and (C) shows an interferogram in August 2019.

Pre- and Post-Ridgecrest Earthquake Sequence SBAS Displacement Grids
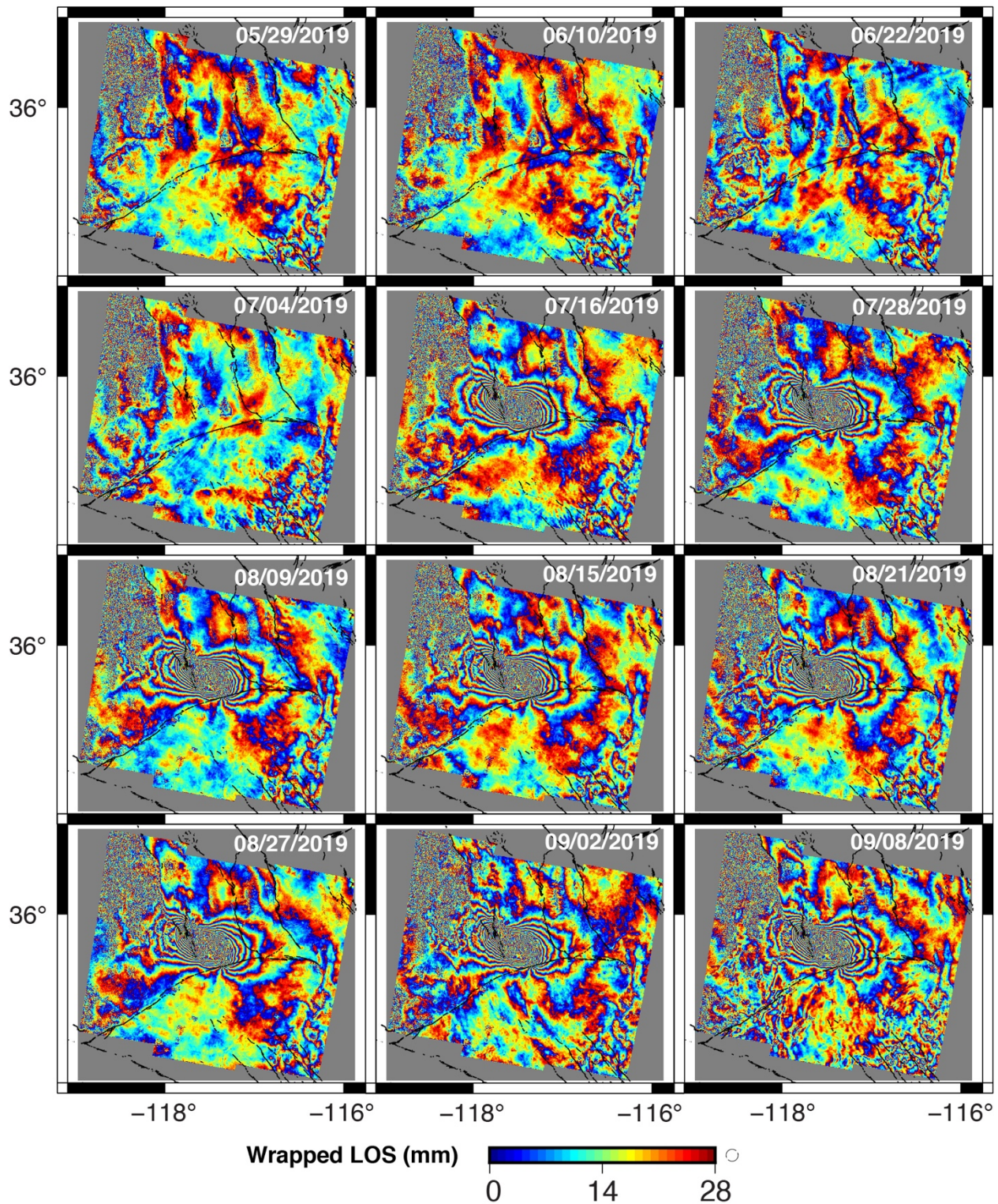
Figure S5. GNSS-corrected InSAR SBAS displacement grids showing Ridgecrest earthquake sequence displacements (all interferograms but the coseismic interferograms are corrected with an Elevation Dependent Atmospheric correction). Holocene and Pleistocene faults are plotted as black lines for reference.
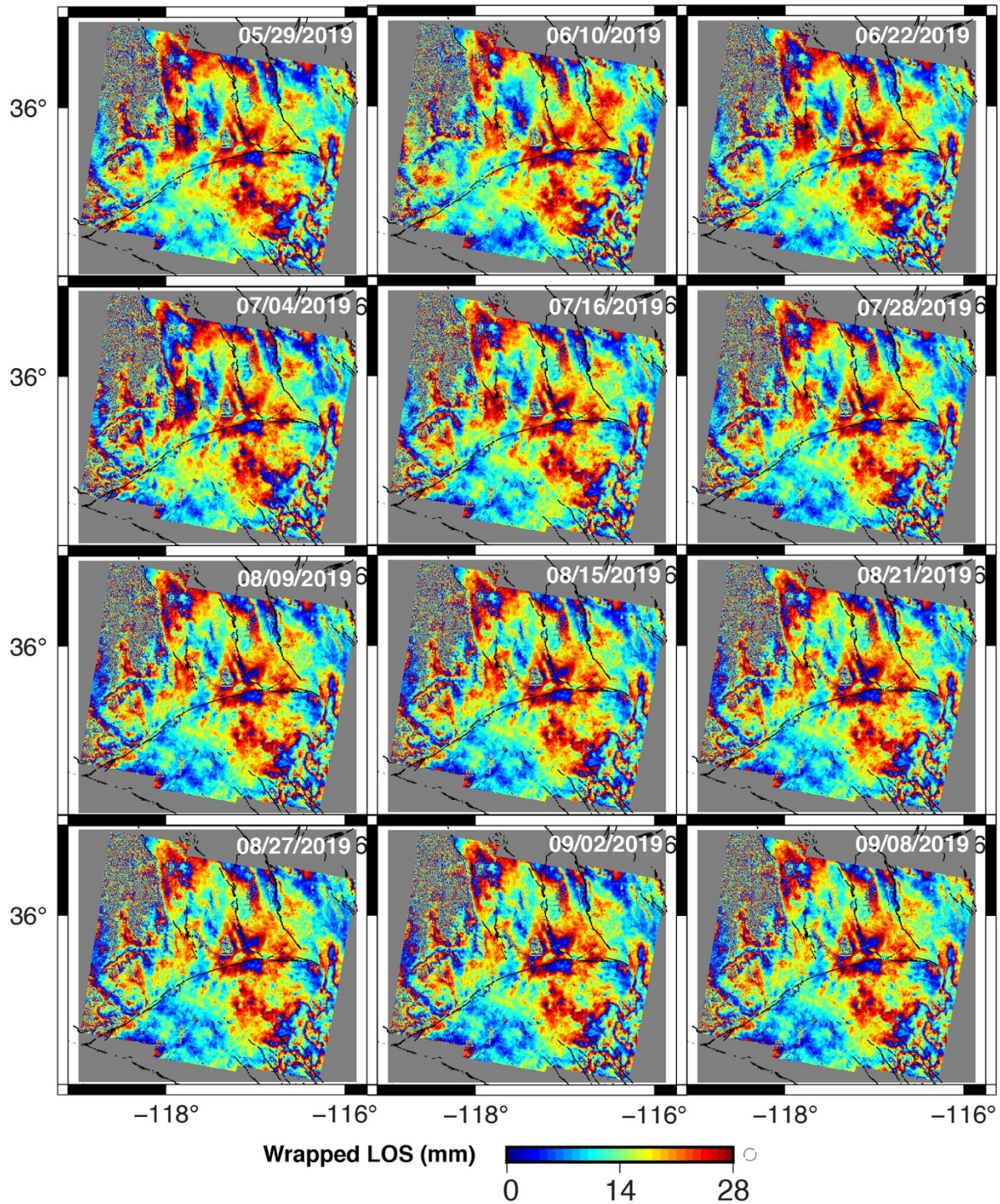
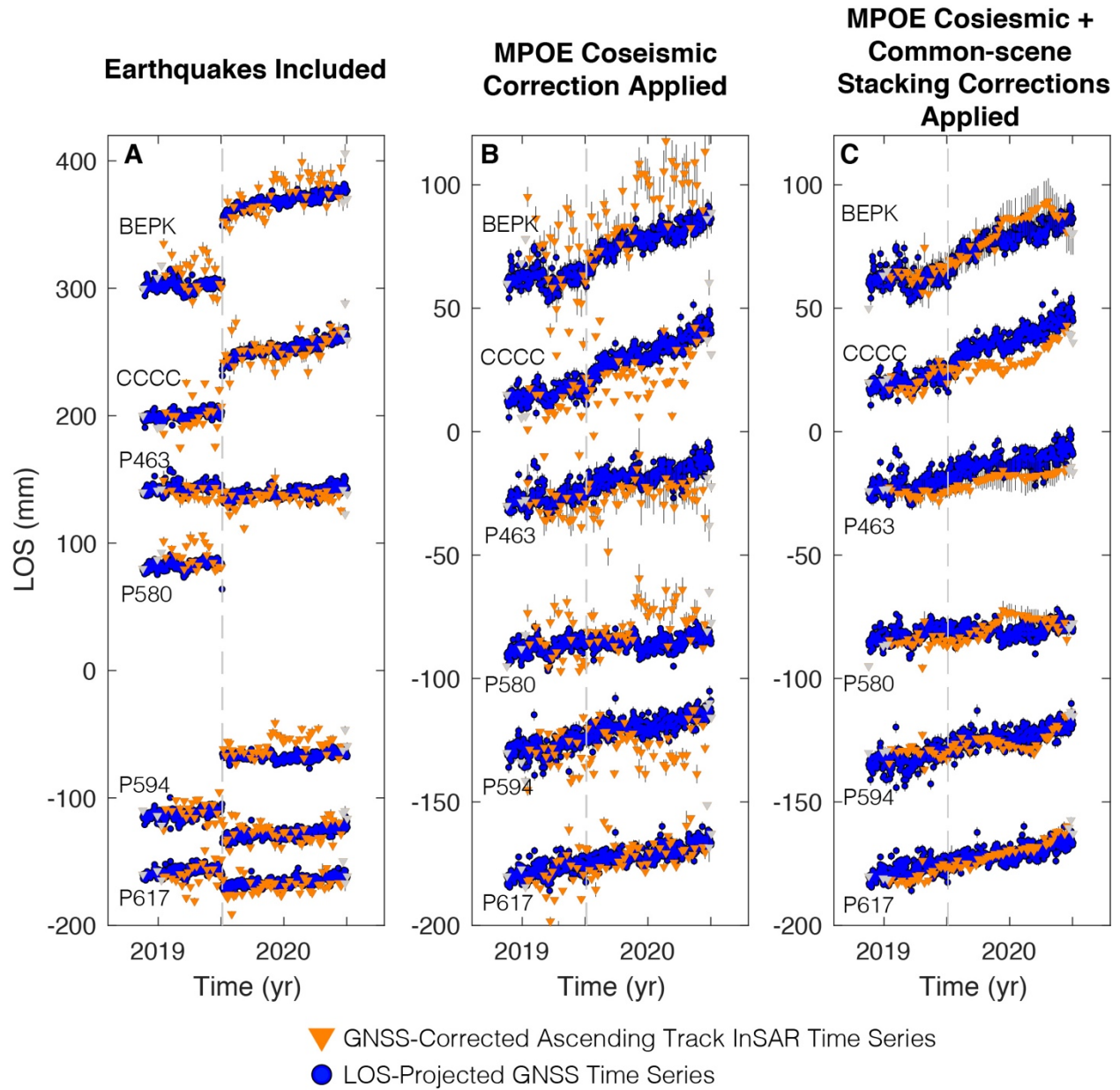**Pre- and Post-Ridgecrest Earthquake Sequence SBAS Displacement Grids: MPOE Coseismic Corrected**
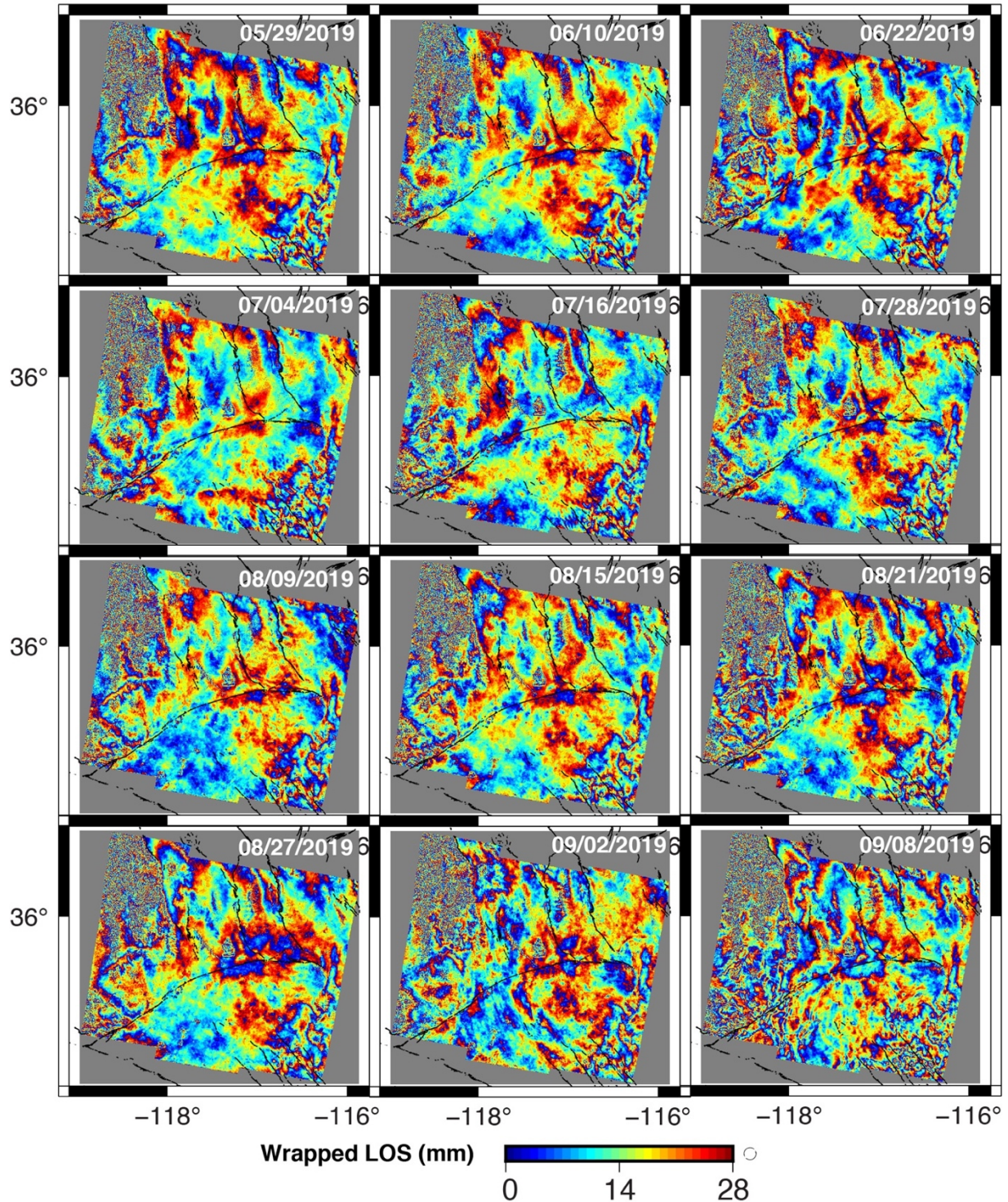
Figure S6. GNSS-corrected, MPOE coseismic-corrected InSAR SBAS displacement grids around the Ridgecrest earthquake events (all interferograms are corrected with an Elevation Dependent Atmospheric correction). Holocene and Pleistocene faults are plotted as black lines for reference.

Pre- and Post-Ridgecrest Earthquake Sequence SBAS Displacement Grids: MPOE Coseismic Corrected, Common-scene Stacking Corrected


Figure S7. GNSS-corrected InSAR SBAS displacement grids showing Ridgecrest earthquake sequence displacements corrected with the MPOE correction and the Common-scene Stacking atmospheric corrections applied (all interferograms are also corrected with an Elevation Dependent Atmospheric correction). Holocene and Pleistocene faults are plotted as black lines for reference.

Figure S8. Ascending track 64 GNSS-corrected InSAR time series plotted on top of GNSS time series in three cases; (A) Time series including the Ridgecrest earthquake sequence offset (with an Elevation Dependent Atmospheric (EDA) Correction applied to all but coseismic interferograms); (B) Results of applying our MPOE coseismic correction with an EDA correction for all interferograms and (C) Results of applying the MPOE coseismic correction, EDA correction and the Common-scene Stacking atmospheric correction. Note scale on panel (A) has a larger LOS range for display purposes.
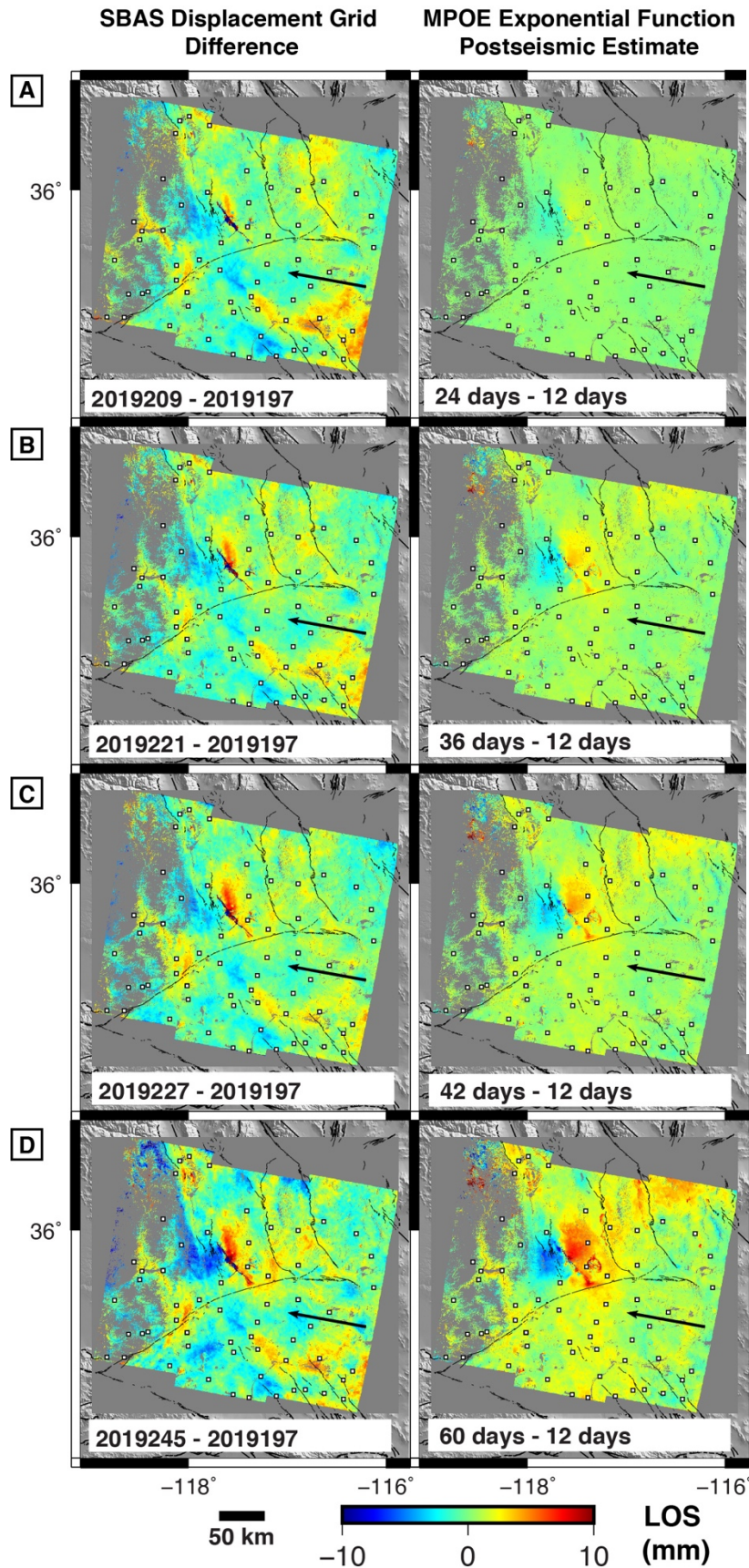
Figure S9. Comparison between SBAS-produced displacement grid differences (Elevation Dependent Atmospheric Correction and Common-scene Stacking atmospheric correction applied) and MPOE exponential postseismic model estimates, for four different time periods; black arrow at right shows the direction of Line-Of-Sight (LOS); (A) shows the 12-day period following the first descending scene after the earthquake (2019_197); (B) shows the 24-day period, (C) shows the 30-day period and (D) shows the 48-day period following day 197.
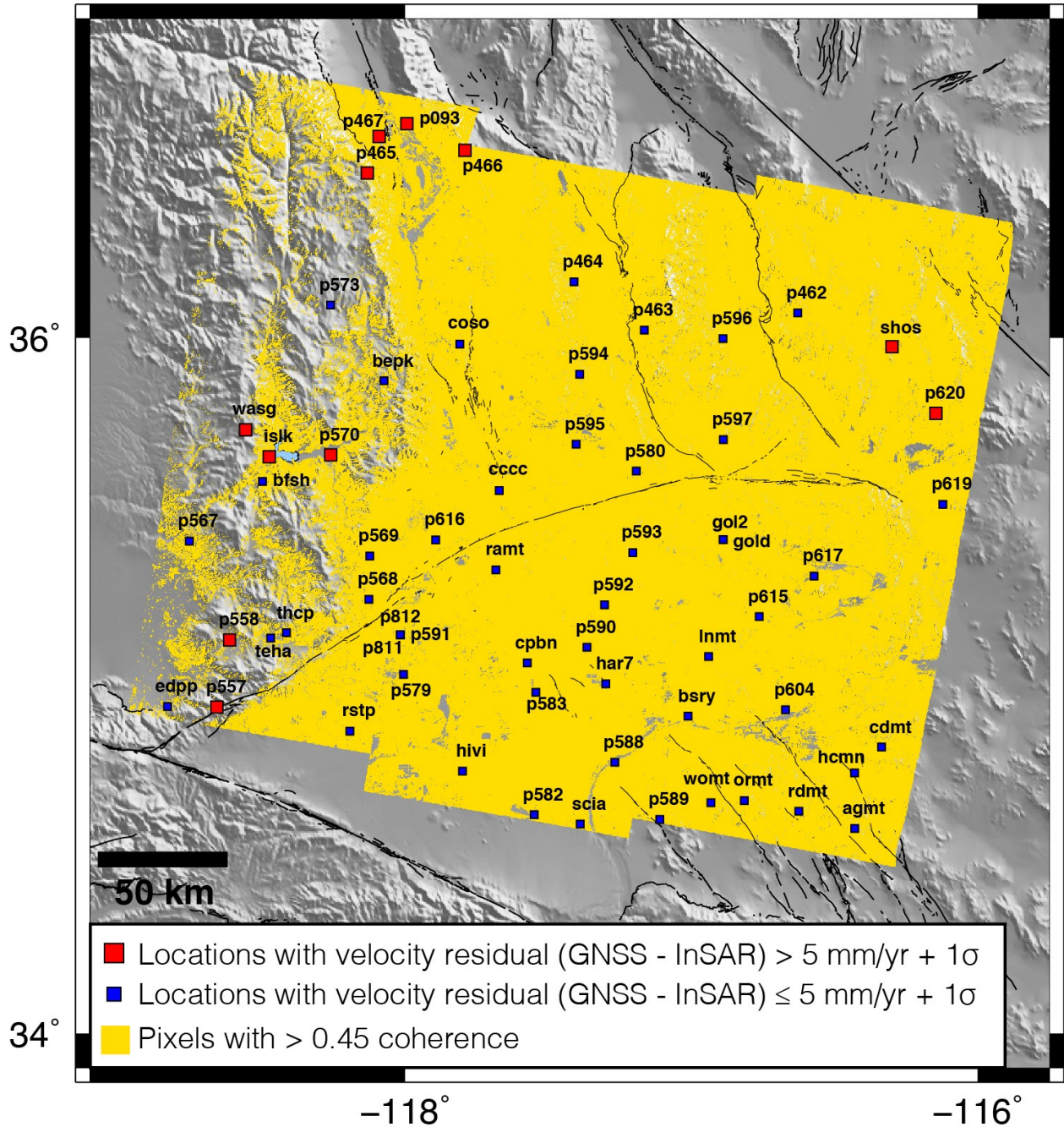
Figure S10. Map showing coherence threshold of 0.45 for descending track 71; station locations exhibiting large (>5 mm/yr + 1σ uncertainties on the velocity estimates) velocity trend residuals between GNSS time series and InSAR time series are colored red, while all other GNSS station locations are colored blue.
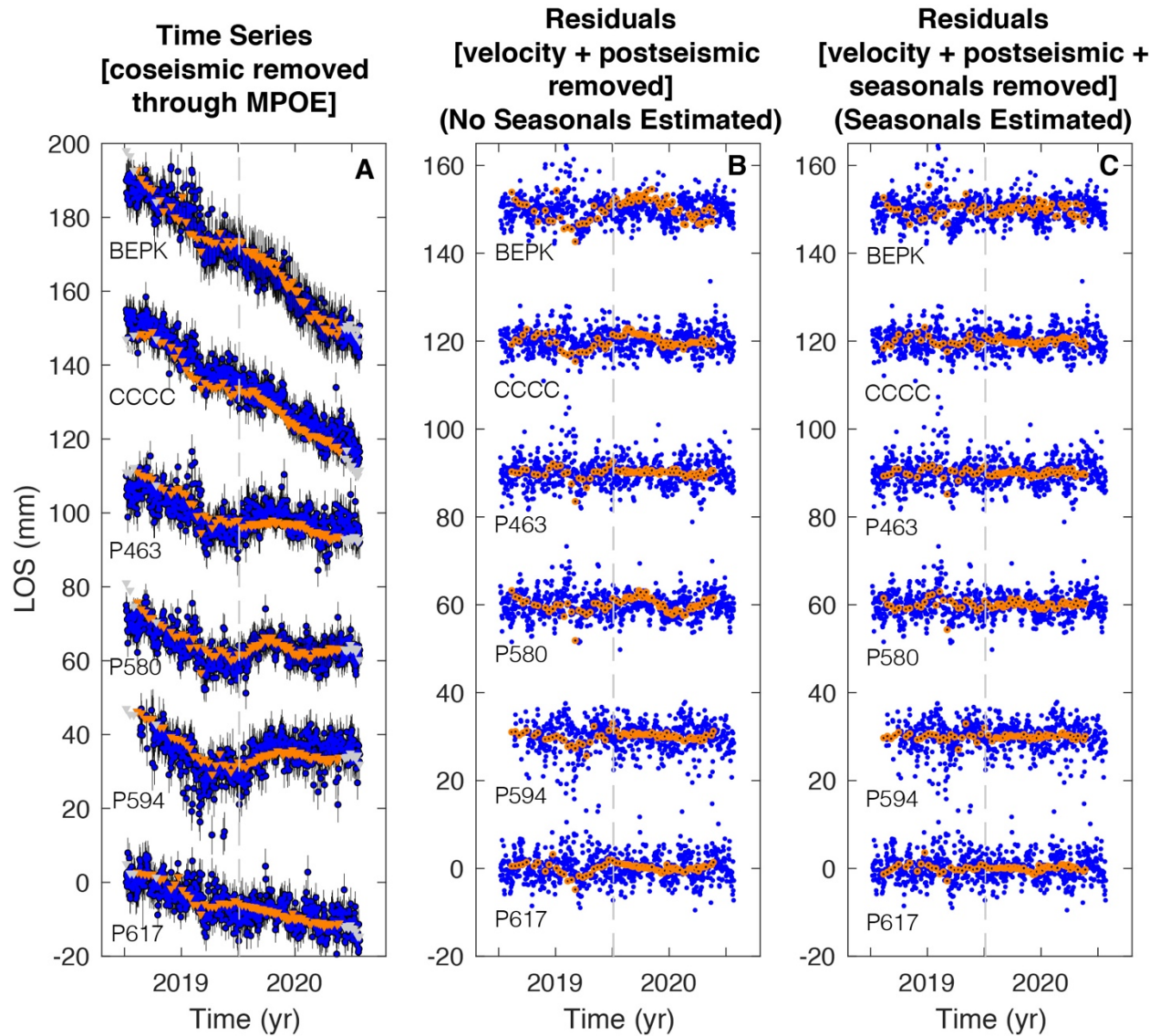
Figure S11. Stacked time series plot showing (A) GNSS time series (blue) and GNSS-corrected, Common-scene Stacking-corrected, coseismic-corrected InSAR time series (orange), (B) time series residuals with velocity and postseismic terms removed (no annual or semi-annual seasonal terms are estimated or removed) and (C) time series residuals with velocity, postseismic, and annual and semi-annual seasonal terms estimated and removed.

13
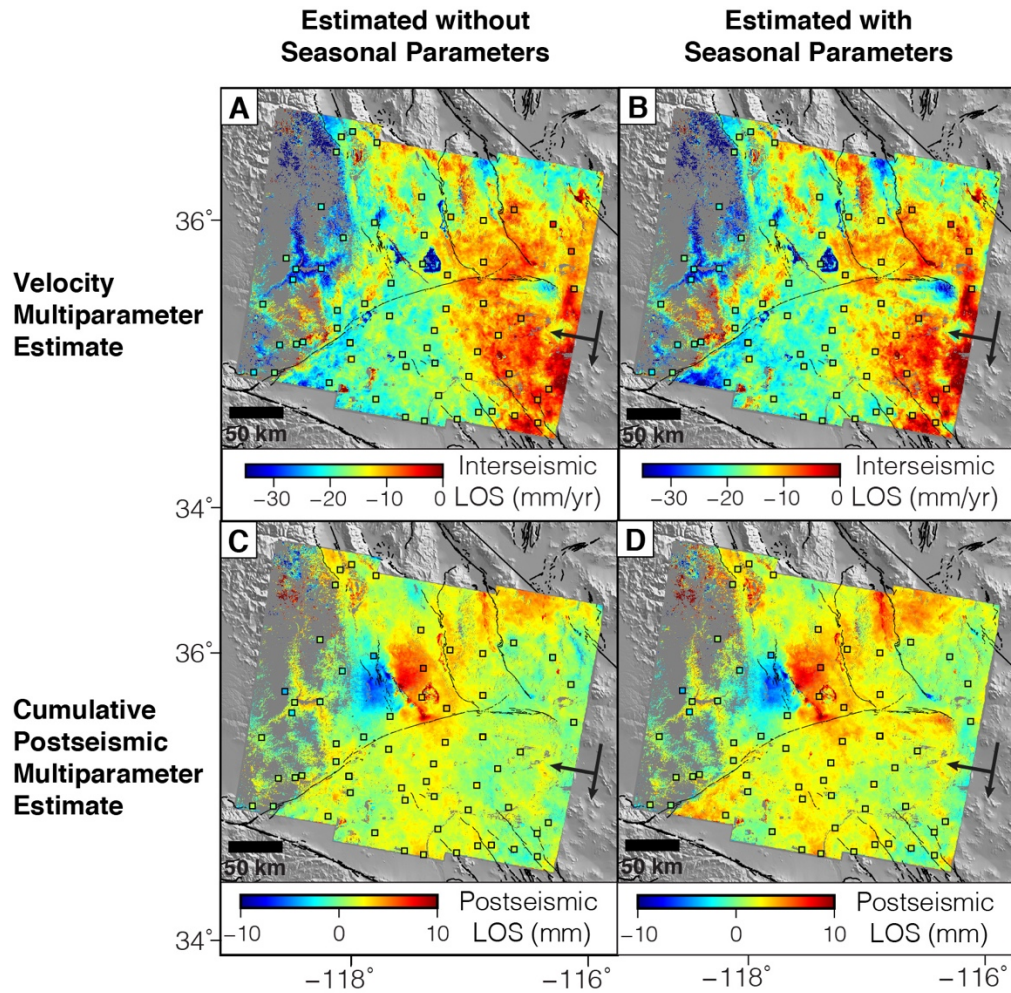
Figure S12. Comparison of multiparameter estimates of velocity and cumulative postseismic, estimated either without seasonal parameters (A,C) or with seasonal parameters (B,D).

Supplementary Datasets

Dataset S1. Coseismic-corrected, GNSS-corrected, Elevation Dependent Atmospheric correction-corrected descending track 071 InSAR time series, extracted and organized by GNSS station location; this is a zip file of 62 station files each with header information including station location, and column names.

Dataset S2. Coseismic-corrected, GNSS-corrected, Elevation Dependent Atmospheric correction-corrected ascending track 064 InSAR time series, extracted and organized by GNSS station location; this is a zip file of 64 station files each with header information including station location, and column names.

Dataset S3. Coseismic-corrected, GNSS-corrected, Elevation Dependent Atmospheric correction-corrected, Common-scene stacking atmospheric-corrected descending track 071 InSAR time series, extracted and organized by GNSS station location; this is a zip file of 62 station files each with header information including station location, and column names.

Dataset S4. Coseismic-corrected, GNSS-corrected, Elevation Dependent Atmospheric correction-corrected, Common-scene stacking atmospheric corrected ascending track 064 InSAR time series, extracted and organized by GNSS station location; this is a zip file of 64 station files each with header information including station location, and column names.